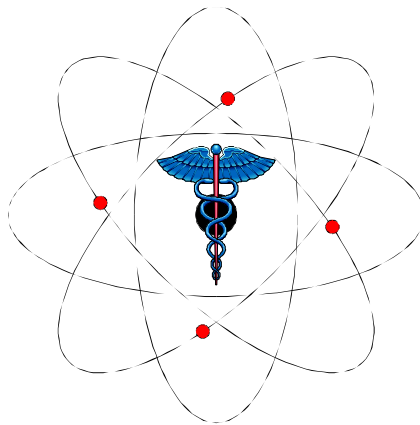


# PARAPET



## Evaluation of Analytic Algorithms

Document: D/4.4/ MILAN/PAGANI-BETTINARDI-GILARDI//  
19 March 2000/1/0.1/

*COMPLETE DELIVERABLE*

Approved by:

.....  
(Author)

V. Friedrich  
(Project manager)

<b>1. INTRODUCTION.....</b>	<b>4</b>
<b>2. THE ANALYTIC ALGORITHMS .....</b>	<b>5</b>
2.1 PROMIS .....	5
2.2 FORE.....	5
<b>3. THE PHANTOMS AND CLINICAL STUDIES USED FOR THE EVALUATION .....</b>	<b>6</b>
<b>3.1 PHANTOM STUDIES .....</b>	<b>6</b>
3.1.1 POINT SOURCES .....	6
3.1.2 UNIFORM CYLINDRICAL PHANTOM .....	6
3.1.3 JASZCZAK PHANTOM .....	6
3.1.4 HOT SPHERE PHANTOM .....	6
3.1.5 HOFFMAN BRAIN PHANTOM .....	7
3.1.6 STRIATA PHANTOM .....	7
3.1.7 HEART PHANTOM.....	7
3.1.8 WHOLE BODY PHANTOM .....	7
<b>3.2 CLINICAL STUDIES .....</b>	<b>8</b>
3.2.1 BRAIN STUDY OF GLUCOSE METABOLISM ( $^{18}\text{F}$ FDG) .....	8
3.2.2 BRAIN STUDY OF NEUROTRANSMISSION SYSTEMS ( $^{18}\text{F}$ FESP) .....	8
3.2.3 HEART STUDY OF GLUCOSE METABOLISM ( $^{18}\text{F}$ FDG) .....	8
3.2.4 WHOLE-BODY STUDY OF GLUCOSE METABOLISM ( $^{18}\text{F}$ FDG) .....	8
<b>3.3 DATA PROCESSING .....</b>	<b>9</b>
<b>4. FIGURES OF MERIT USED FOR THE EVALUATION .....</b>	<b>10</b>
<b>4.1 SPATIAL RESOLUTION.....</b>	<b>10</b>
<b>4.2 COEFFICIENT OF VARIATION.....</b>	<b>10</b>
<b>4.3 CONTRAST .....</b>	<b>10</b>
<b>4.4 RADIOACTIVITY CONCENTRATION RATIO .....</b>	<b>10</b>
<b>4.5 FOMs and ROIs.....</b>	<b>11</b>
4.5.1 PHANTOM STUDIES .....	11
4.5.2 CLINICAL STUDIES .....	14
<b>5. RECONSTRUCTION CONFIGURATIONS .....</b>	<b>17</b>
<b>5.1 PROMIS.....</b>	<b>17</b>

<b>5.2 FORE .....</b>	<b>17</b>
<b>5.3 2D FBP.....</b>	<b>18</b>
<b>6. RESULTS .....</b>	<b>19</b>
<b>6. 1 PHANTOM STUDIES.....</b>	<b>19</b>
6.1.1.POINT SOURCES .....	19
6.1.2 UNIFORM CYLINDRICAL PHANTOM .....	19
6.1.3 JZAZACK PHANTOM.....	21
6.1.4 HOT SPHERE PHANTOM.....	23
6.1.5 HOFFMAN BRAIN PHANTOM.....	26
6.1.6 STRIATA PHANTOM .....	28
6.1.7 HEART PHANTOM .....	30
6.1.8 WHOLE BODY PHANTOM.....	32
<b>6.2 CLINICAL DATA .....</b>	<b>34</b>
6.2.1 BRAIN STUDIES OF GLUCOSE METABOLISM ( $^{18}\text{F}$ FDG) .....	34
6.2.2 BRAIN STUDIES OF NEUROTRANSMISSION SYSTEMS (FESP) .....	36
6.2.3 HEART STUDIES OF GLUCOSE METABOLISM ( $^{18}\text{F}$ FDG) .....	38
6.2.4 WHOLE-BODY STUDIES OF GLUCOSE METABOLISM ( $^{18}\text{F}$ FDG) .....	40
<b>7. CONCLUSIONS .....</b>	<b>44</b>
<b>8. REFERENCES.....</b>	<b>45</b>

## 1. INTRODUCTION

Aim of this document is to report the evaluation of the 3D analytic reconstruction algorithms developed within WP 4 of the PARAPET project: PROMIS [PAR4.2] and FORE [PAR4.3].

In order to make this document self-consistent PROMIS and FORE algorithms are briefly described in Section 2, with respect to the choice of reconstruction parameters.

The PROMIS and FORE algorithms were used to reconstruct a representative set of experimental phantom and clinical data derived from the “Acquisition Data Library” created within the PARAPET Project [PAR3.2]. The data used for the evaluation are described in Section 3 of this Document. When data were recorded in both 2D and 3D modalities, 2D and 3D reconstruction algorithms were used, in order to compare image quality in 2D and 3D PET, respectively.

Section 4 summarizes the Figures of Merit (FOM) [PAR3.1] measured for each phantom and clinical study, in order to assess the quality of the reconstructed images and the performance of the reconstruction algorithm used.

Reconstruction algorithms were used in different set-up, in terms of reconstruction parameters (filters, filter parameters). The different reconstruction configurations are discussed in Section 5 for both PROMIS and FORE.

The results of evaluation in terms of measured FOMs and image quality are reported and discussed in Section 7.

## 2. THE ANALYTIC ALGORITHMS

### 2.1 PROMIS

The 3D reprojection algorithm of Kinahan and Rogers [Kin89] – also called PROMIS (Projection of Missing Data) – is the most widely used 3D reconstruction algorithm. This algorithm is based on an exact method whereby the data incompleteness inherent in the 3D acquisition method is addressed by forward projection. A comprehensive and theoretical description of the PROMIS algorithm is provided in [PAR4.2]. The parameters characterizing each reconstruction configuration and the possible choices are:

- Colsher Transaxial filter:  
Window: Rectangular, Hanning, Hamming
- Colsher Axial filter:  
Window: Rectangular, Hanning, Hamming
- Cut-off for the Transaxial filter: 0 - 0.5
- Cut-off for the Axial filter: 0 - 0.5

### 2.2 FORE

The Fourier rebinning algorithm – also called FORE – is one of the proposed algorithms for three-dimensional image reconstruction in which oblique sinograms are rebinned into direct (2D) sinograms using a frequency/distance relationship given in the Fourier space [Def97]. This allows 2D processing of the 3D data, thus speeding up the reconstruction by an order of magnitude. A comprehensive and theoretical description of the FORE algorithm is provided in [PAR4.3]. The parameters characterizing each reconstruction configuration and the possible choices are

- Rebinning  
smallest angular frequency index  $k_{\min}$ : 0 - 10  
smallest transaxial frequency index  $w_{\min}$ : 0 - 10  
index for consistency  $k_c$ : 0 - 10  
 $\Delta_{\max}$  for small  $\omega$ : 0-10
- 2D FBP filter  
window: Rectangular, Hanning, Hamming

cut-off: 0 - 0.5

### **3. THE PHANTOM AND CLINICAL STUDIES USED FOR THE EVALUATION**

Data used for evaluation of the analytic algorithms were collected by the GE Advance scanner at H S.Raffaele Institute in Milan.

#### **3.1 PHANTOM STUDIES**

##### **3.1.1 POINT SOURCES (PS)**

Six PSs of  $^{18}\text{F}$  were positioned at different locations in the central plane of the PET scanner (0, 5, 10, 15, 20, 25 cm off centre). PET scans of the PSs were repeated in two external planes (3.5 and 7cm off centre). In this evaluation, the set of PSs in the central plane was considered.

##### **3.1.2 UNIFORM CYLINDRICAL PHANTOM (UCY)**

A UCY phantom (diameter = 20cm, height = 20cm) was filled with a homogeneous solution of water and  $^{18}\text{F}$  (4.4 kBq/cc). The phantom was positioned in the centre of the Field of View (FOV). In order to reproduce clinical conditions, a high counting statistics PET study (HS:  $\approx 200$  Mcounts as in a 3D PET  $^{18}\text{F}$ FDG brain study) and a low counting statistics PET study (LS:  $\approx 10$  Mcounts as in a 3D PET  $\text{H}_2^{15}\text{O}$  brain study) were considered.

##### **3.1.3 JASZCZAK PHANTOM (JZA)**

The JZA phantom consists of a cylinder (diameter = 20cm, height = 20cm) with an insert of six sectors. Each sector is composed of cold rods, whose size changes in each sector: 12.7, 11.1, 9.5, 8.4, 6.4, 4.5 mm. The JZA phantom, with the cold rods insert in, was filled with a homogeneous solution of water and  $^{18}\text{F}$  (15.1MBq in the phantom at the study time). The phantom was positioned in the centre of the scanner FOV. In order to reproduce clinical conditions, a high counting statistics (HS:  $\approx 200$  Mcounts) and a low counting statistics (LS:  $\approx 50$  Mcounts) study were considered.

##### **3.1.4 HOT SPHERE PHANTOM (HS)**

The HS phantom consists of a uniform cylinder (diameter = 20 cm, height = 20 cm) with spherical inserts. The sphere diameters were: 38, 31.5, 25.5, 18.5, 16, 13 and 9.5mm, respectively. The HS phantom was filled with a homogeneous solution of water and  $^{18}\text{F}$ . Radioactivity concentration ratio between spheres and the surrounding background at the time of the PET scan was 1.5 for the three larger spheres, 2.8 for the two

intermediate and 3.6 for the two smaller. The phantom was positioned in the centre of the scanner FOV. A high counting statistics (HS:  $\approx 200$  Mcounts) and a low counting statistics (LS:  $\approx 18$  Mcounts) study were considered.

### **3.1.5 HOFFMAN BRAIN PHANTOM (HB)**

The 3D HB phantom (Data Spectrum Corporation) simulates the radioactivity distribution of a cerebral PET study with  $^{18}\text{F}$ -Fluorodeoxyglucose ( $^{18}\text{F}$ FDG) (glucose metabolism) or with  $\text{H}_2^{15}\text{O}$  (blood flow). The phantom was filled with a homogeneous solution of water and  $^{18}\text{F}$  (22.6 MBq in the phantom at the study time). The compartments of the phantom are such to create a radioactivity concentration ratio of 4 between gray and white matter, to reproduce the functional ratio of 4 in terms of glucose metabolism and blood flow in normal brain. The phantom was positioned in the center of the scanner FOV. In order to reproduce clinical conditions, a high counting statistics (HS:  $\approx 200$  Mcounts) and a low counting statistics (LS:  $\approx 50$  Mcounts) study were considered.

### **3.1.6 STRIATA PHANTOM (ST)**

The ST phantom (RSD Radiology Support Devices, Long Beach, CA) simulates the radioactivity distribution of a cerebral PET study with a neurotransmission tracer (e.g.  $^{18}\text{F}$ Fluoroethylspiperone,  $^{18}\text{F}$ FESP). The phantom was filled with a homogeneous solution of water and  $^{18}\text{F}$ . Radioactivity concentration ratio between basal ganglia (BG) and background (Bkg) at the time of the PET scan was 3.84 (43.4 kBq/cc in the BG compartment and 11.3 kBq/cc in the Bkg). The phantom was positioned in the center of the scanner FOV. In order to reproduce clinical conditions typical of a neurotransmission study (e.g. with  $^{18}\text{F}$ FESP), counting statistics was 33 Mcounts. To note, this phantom was not available in the PARAPET consortium, but data, collected by a GE Advance PET scanner, were kindly provided by the Turku PET Centre.

### **3.1.7 HEART PHANTOM (H)**

The H phantom simulates the radioactivity distribution of a heart PET study (e.g. study of glucose metabolism with  $^{18}\text{F}$ FDG). The phantom was filled with homogeneous solutions of water and  $^{18}\text{F}$ . Radioactivity concentration ratio in the Left Ventricle (LV) wall with respect to the LV cavity was 1.74. In order to simulate an ischemic lesion, a cold region was created on the LV wall (plexiglass insert, 10 mm size). In order to reproduce clinical conditions, a high counting statistics (HS:  $\approx 200$  Mcounts) and a low counting statistics (LS:  $\approx 5$  Mcounts) study were considered.

### **3.1.8 WHOLE BODY PHANTOM (WB)**

The WB phantom simulates the radioactivity distribution of a Whole Body PET  $^{18}\text{F}$ FDG study. It is composed of a large container (simulating the shape of the thorax) with six hot spheres inside, supported on cold cylindrical rods. The size of the spheres is as in the HS phantom. The spheres were not co-axial. They were positioned in different locations in the container, to simulate regions of high radioactivity concentration as found in clinical oncology studies in presence of metastatic lesions. The spheres were filled with homogeneous solutions of water and  $^{18}\text{F}$ , while the container with the faster decaying  $^{11}\text{C}$ . The radioactivity concentration ratios in the compartments of the phantom were thus changing with time and a dynamic acquisition provided a set of data characterized by different contrast in the spheres with respect to the background. In this evaluation a single WB phantom study was considered, with a radioactivity concentration ratio of 7.5. Counting statistics was 10.78 Mcounts.

## **3.2. CLINICAL STUDIES**

### **3.2.1 BRAIN STUDY OF GLUCOSE METABOLISM ( $^{18}\text{F}$ FDG)**

A PET  $^{18}\text{F}$ FDG brain study allows the assessment of regional cerebral glucose metabolism and represents one of the most relevant clinical PET examination for the diagnosis of neurological diseases (e.g. cerebrovascular disease, epilepsy, dementia). A  $^{18}\text{F}$ FDG brain study in a patient affected by brain tumor and previously treated by radiotherapy was considered. The  $^{18}\text{F}$ FDG PET study was performed to allow the differentiation between tumor recurrence and radionecrosis. Acquisition protocol was as follows: 3D and 2D PET scans (10min) were sequentially recorded, starting 45 min after i.v. injection of  $\approx 300$  MBq of  $^{18}\text{F}$ FDG. A post-injection transmission scan was performed, to allow measured attenuation correction.

### **3.2.2 BRAIN STUDY OF NEUROTRANSMISSION SYSTEMS ( $^{18}\text{F}$ FESP)**

$^{18}\text{F}$ FESP is a tracer of the  $\text{D}_2$  dopaminergic receptors, principally localized in the basal ganglia, and of the  $5\text{HT}_2$  serotonergic receptors, prevalent in the cortical structures.  $^{18}\text{F}$ FESP PET studies have important applications in the diagnosis of psychiatric diseases. A  $^{18}\text{F}$ FESP PET study in a normal subject was considered (2D and 3D data available). Acquisition protocol was as follows: 2D and 3D PET scans (10min) were sequentially recorded, starting 20 min after i.v. injection of  $\approx 150$  MBq of  $^{18}\text{F}$ FESP. A post-injection transmission scan was performed, to allow measured attenuation correction.



### **3.2.3 HEART STUDY OF GLUCOSE METABOLISM ( $^{18}\text{F}$ FDG)**

A PET  $^{18}\text{F}$ FDG heart study of glucose metabolism allows the assessment of myocardial viability and represents a relevant clinical application of PET in the diagnosis of myocardial ischemic diseases. A PET heart  $^{18}\text{F}$ FDG study was considered (3D data available) in a patient affected by anterior myocardial. Acquisition protocol was as follows: a 3D PET scan (10min) was recorded, starting 45 min after i.v. injection of  $\approx 300$  MBq of  $^{18}\text{F}$ FDG. A post-injection transmission scan was performed, to allow measured attenuation correction.

### **3.2.4 WHOLE-BODY STUDY OF GLUCOSE METABOLISM ( $^{18}\text{F}$ FDG)**

A PET  $^{18}\text{F}$ FDG whole-body study allows the assessment of glucose metabolism in the human body for the detection of primary tumours as well as of metastatic lesions, presenting with an increased metabolic activity (increased radioactivity uptake) with respect to normal tissues. A  $^{18}\text{F}$ FDG whole-body pathological study was considered, consisting of 6 adjacent PET scans to cover an extended part of the body. A specific PET scan out of the 6 was selected, showing metastatic lesions (2D and 3D data available). A post-injection transmission scan was performed, to allow measured attenuation correction.

## **3.3 DATA PRE-PROCESSING**

For all phantom and clinical studies, projection data were pre-corrected for detection efficiency, scatter, random coincidences, attenuation. Measured attenuation correction was performed by transmission measurement.

## 4. FIGURES OF MERIT USED FOR THE EVALUATION

### 4.1 SPATIAL RESOLUTION

The FOM Spatial Resolution was defined on images of a point source as the Full Width Half Maximum (FWHM) of the spatial distribution profile drawn across the reconstructed image of the point source. For each point source image in different locations in the scanner FOV, FWHM was defined on both tangential and radial distribution profiles.

### 4.2 COEFFICIENT OF VARIATION

The FOM Coefficient of Variation was measured on images of a large object of uniform activity (e.g. UCY Phantom). Coefficient of Variation was estimated on the region of uniform activity as the standard deviation of the estimated activity divided by the mean estimated activity in that region:

$$CV = (S (v_i - m)^2 / N)^{1/2} / m$$

where  $v_i$  are the voxel values (voxels lying entirely in the ROI),  $m$  is the mean value for the ROI and  $N$  is the number of voxels.  $CV$  is positive and should be as small as possible.

### 4.3 CONTRAST C

The FOM Contrast ( $C$ ) was measured on images presenting with “cold” regions in a radioactive background. Contrast was calculated as

$$C = (m_{bkg} - m_{cold}) / m_{bkg}$$

where  $m_{bkg}$  and  $m_{cold}$  are the mean values for ROIs drawn on the radioactive background and the cold region, respectively.

When the cold regions are not radioactive, the theoretical value for  $C$  is 1.

### 4.4 RADIOACTIVITY CONCENTRATION RATIO (RCR)

The FOM Radioactivity Concentration Ratio (RCR) was measured on images of complex phantoms and clinical studies as the ratio between the estimated radioactivity concentrations in two defined compartments in phantom studies and in two defined anatomical structures in clinical studies.

$$RCR = m_1 / m_2$$

where  $m_1$  and  $m_2$  are the mean values for ROIs drawn on the two compartments or structures.

## 4.5 FOMs and ROIs

### 4.5.1 PHANTOM STUDIES

- *JZA Phantom - C*

In the JZA phantom studies, the FOM Contrast  $C$  was calculated in the cold rods with respect to the radioactive background. ROIs were drawn as shown in Figure 4.1 on the radioactive background and on the cold rods in all sectors, with the exception of the smallest one (4.8mm), where the detection of the cold rod was difficult due to the small size. ROIs size was 3.7 mm for the background and 75% of the real size for the cold rods.  $m_{bkg}$  and  $m_{cold}$  were estimated as average over all background ROIs and all cold rods ROIs, respectively.

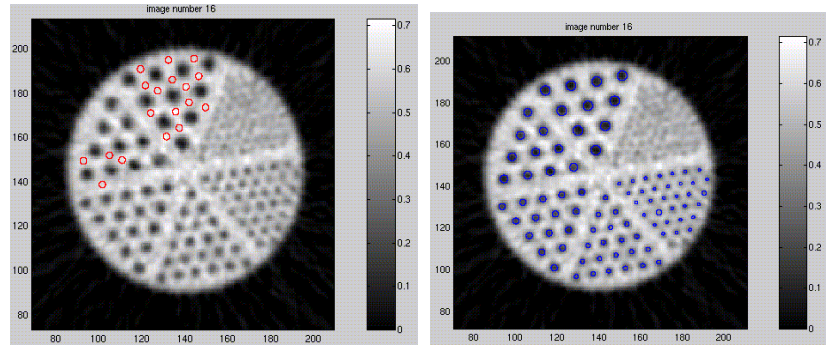


**Figure 4.1** ROIs drawn on images of the Jazszczak phantom to calculate background radioactivity  $m_{bkg}$  (left) and to calculate 'apparent' radioactivity in the cold rods  $m_{cold}$  (right)

- *HS Phantom - RCR*

In the HS phantom studies, the FOM RCR was calculated for the seven spheres in the phantom. For each sphere, circular ROIs with the same size of the sphere were drawn to estimate  $m_1$  (Figure 4.2). A large irregular ROI was drawn to estimate  $m_2$ .

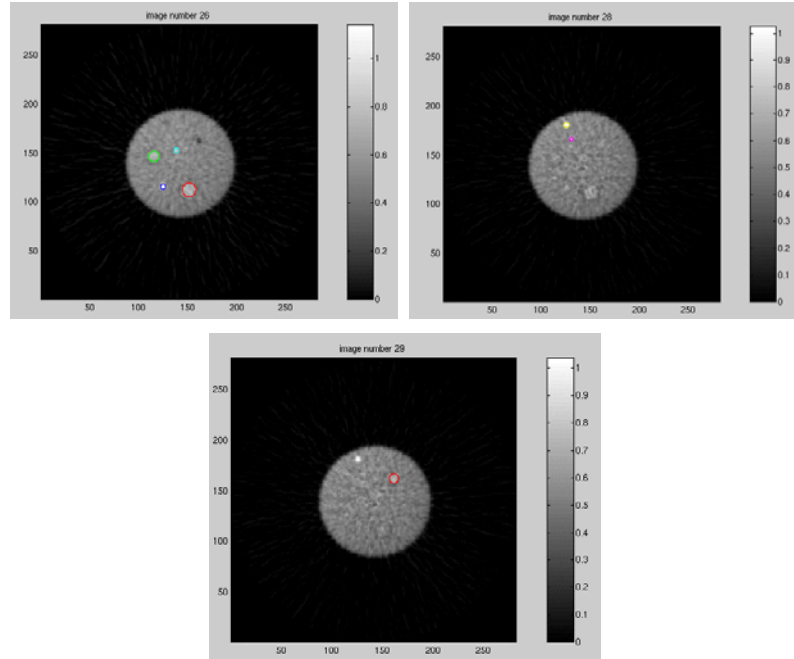


**Figure 4.2** ROIs drawn on images of the HS phantom to calculate radioactivity in the hot spheres

- *HB phantom - RCR and C*

In the HB phantom studies, the following FOMs were calculated:

- RCR between Gray matter (GM) and White matter (WM),
- C in the region corresponding to the Cerebrovascular Fluid (CSF, radioactivity concentration is zero) with respect to GM.

ROIs were drawn in various slices on the GM, WM and CSF, as shown in Figure 4.3.

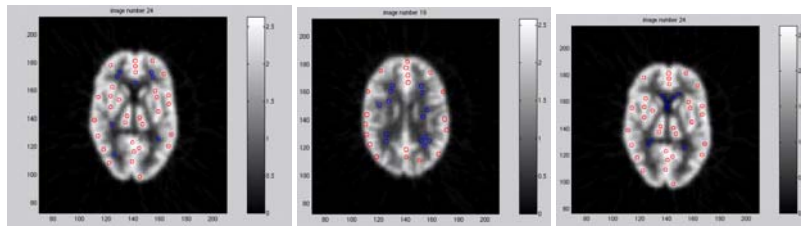


**Figure 4.3** HB phantom. ROIs drawn on two representative images, to calculate radioactivity concentration in GM (red ROIs in slice#24, left and right; slice#19, centre), WM (blue ROIs in slice#19, centre, and in slice #24, right) and CSF (blue ROIs in slice#24, right)

- *ST phantom - RCR*

In the ST phantom the FOM RCR was calculated between radioactivity concentration in the basal ganglia (caudate and putamen) and the surrounding background. ROIs were drawn as shown in Figure 4.4.

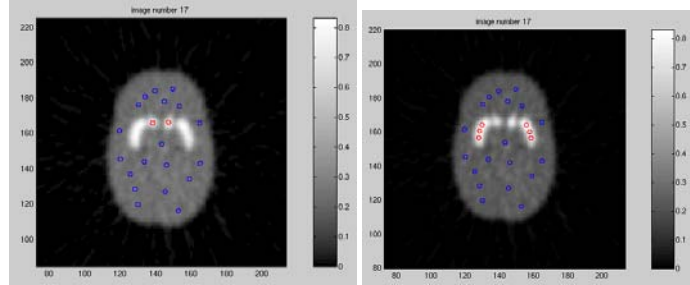


**Figure 4.4** *ST phantom. ROIs drawn on a representative image (slice#17) to calculate radioactivity concentration in the basal ganglia and in the surrounding background. Red ROIs on the caudate (left) and the putamen (right)*

- *Heart phantom - RCR and C*

In the heart phantom studies, the following FOMs were calculated:

- RCR between radioactivity concentration in the Left Ventricle (LV) wall and the LV cavity.
- C in the cold lesion with respect to the LV wall.

ROIs were drawn as shown in Figure 4.5.

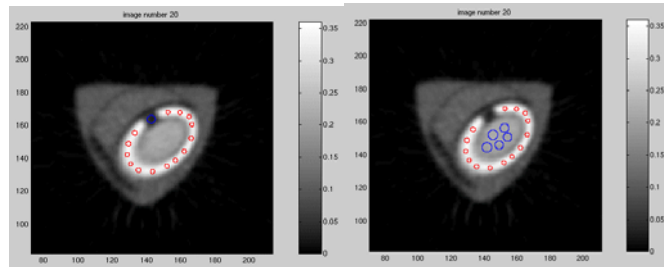


**Figure 4.5** *Heart phantom. ROIs drawn on a representative image (slice#20), to calculate radioactivity concentration in the LV wall and in the cold lesion (left) and to calculate radioactivity concentration in the LV wall and cavity (right)*

- *Whole Body Phantom - RCR*

In the Whole Body phantom studies, the FOM RCR was calculated between radioactivity concentration in the radioactive spheres with respect to the surrounding background. ROIs were drawn on the radioactive spheres as shown in Figure 4.6.

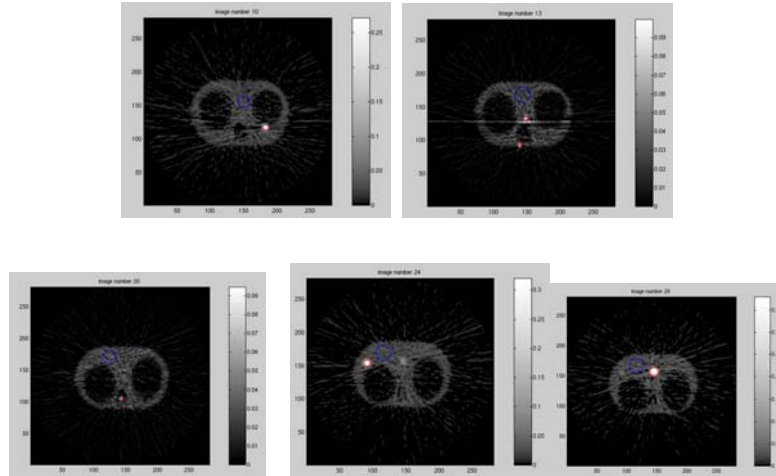


**Figure 4.6** Whole Body phantom. ROIs drawn to calculate radioactivity concentration in the six spheres

- Whole Body Phantom - RCR
- 

In the Whole Body phantom studies, the FOM RCR was calculated between radioactivity concentration in the radioactive spheres with respect to the surrounding background. ROIs were drawn on the radioactive

#### 4.5.2 CLINICAL STUDIES

- $^{18}\text{F}$ FDG brain study - RCR and C

In the  $^{18}\text{F}$ FDG brain study, the following FOMs were calculated:

- RCR between Gray matter (GM) and White matter (WM),
- C in the Cerebrovascular Fluid (CSF) with respect to GM.

ROIs were drawn in various slices on GM, WM and CSF as shown in Figure 4.7.

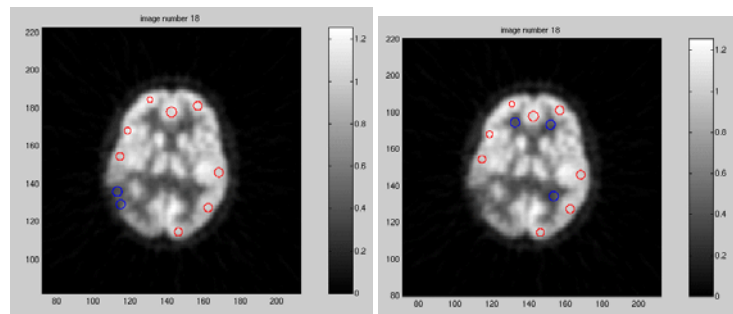


**Figure 4.7**  $^{18}\text{F}$ FDG brain study. ROIs drawn on a representative image (slice #18), to calculate radioactivity concentration in the gray matter (red ROIs), in the white matter (blue ROIs, right) and in the pathological lesion (blue ROIs, left)

- $^{18}\text{F}$ FESP brain study - RCR

In the  $^{18}\text{F}$ FESP brain study the FOM RCR was calculated between the basal ganglia and the cerebellum (Binding Index, BI). ROIs were drawn as shown in Figure 4.8.

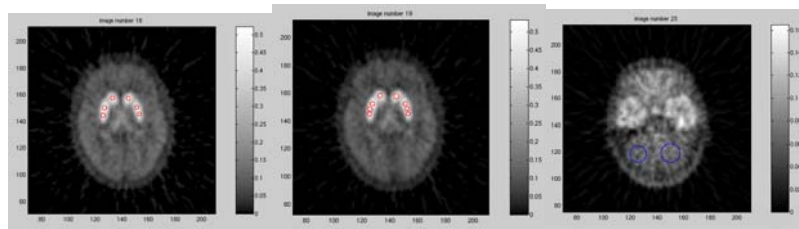


**Figure 4.8** ROIs drawn on two representative images (slice#18 and 19) of the  $^{18}\text{F}$ FESP study, to calculate radioactivity concentration in the basal ganglia (left) and in the cerebellum (right)

- $^{18}\text{F}$ FDG heart study - RCR

In the  $^{18}\text{F}$ FDG heart study, the following FOMs were calculated:

- RCR between Left Ventricle (LV) wall and LV cavity
- C in an ischemic lesion with respect to LV

ROIs were drawn as shown in Figure 4.9.

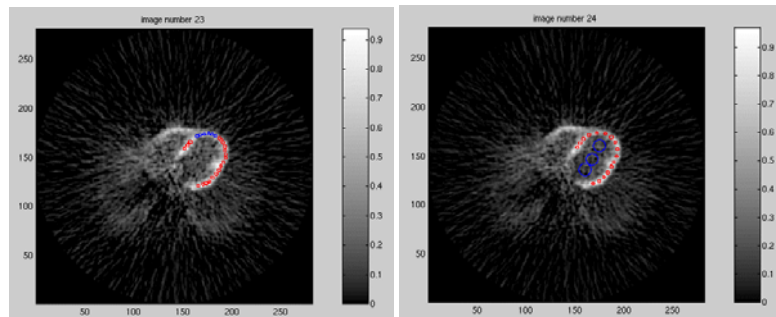


**Figure 4.9**  $^{18}\text{F}$ FDG Heart study. ROIs drawn on a representative image (slice#28), to calculate radioactivity concentration in the LV wall and cavity. Blue ROIs on the left image correspond to an ischemic lesion

- $^{18}\text{F}$ FDG Whole Body study - RCR

In the  $^{18}\text{F}$ FDG Whole Body study, the FOM RCR was calculated between the pathological lesions presenting with high uptake of the radiotracer and the surrounding background. ROIs were drawn as shown in Figure 4.10.

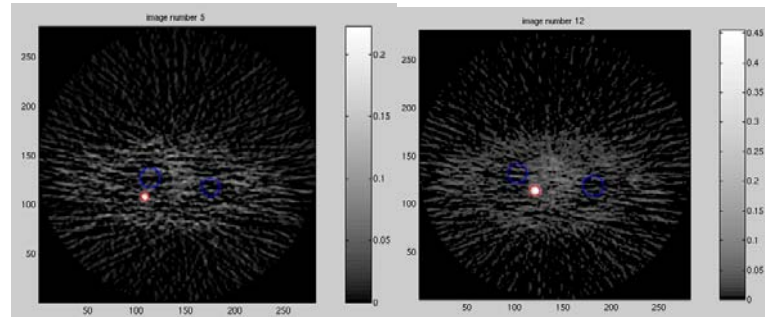


**Figure 4.10**  $^{18}\text{F}$ FDG Whole Body study. ROIs drawn on two representative image (slice#5 and 12), to calculate radioactivity concentration in the hot lesion and in the surrounding background



## 5. RECONSTRUCTION CONFIGURATIONS

### 5.1 PROMIS

In all PROMIS reconstructions the following parameters were adopted:

- Reconstructed FOV: 55cm,
- Image matrix: 281x281 (pixel size = 1.97mm)

Three reconstruction configurations were considered, as follows:

		Colsher Transaxial window	Cut-off	Colsher Axial window	Cut-off
1	RR	Rectangular	0.5	Rectangular	0.5
2	HR	Hanning	0.5	Rectangular	0.5
3	HH	Hanning	0.5	Hanning	0.5

These three reconstruction configurations were chosen to cover reconstruction set-ups representative of those used for clinical studies. In particular:

- Condition 1 (RR) allows the best resolution to be maintained in the images but with high noise particularly in the case of low counting statistics data.
- Condition 2 (HR) represents a good compromise in terms of noise reduction in the transaxial plane, while maintaining high resolution in the axial direction.
- Condition 3 (HH) represents a typical set up used in clinical applications, when low counting statistics data have to be reconstructed, privileging noise reduction, at the expense of spatial resolution.

### 5.2 FORE

In all FORE reconstructions the following parameters were adopted:

- Reconstructed FOV: 55cm

- Image matrix: 281x281 (pixel size = 1.97mm)
- Rebinning parameters:  $w_{\min} = 2$ ,  $k_{\min} = 2$ ,  $k_c = 4$ ,  $\Delta_{\max} = 4$

The following 2D FBP reconstruction configurations were considered:

		Window	Cut-off
1	FR	Rectangular	0.5
2	FH	Hanning	0.5

These two reconstruction configurations were chosen to investigate two different situations:

- Condition 1 (FR) allows the best resolution to be maintained in the images but with high noise particularly in the case of low counting statistics data.
- Condition 2 (FH) represents a typical set up used in clinical applications, privileging noise reduction to spatial resolution.

### 5.3 2D FBP

When 2D data were available, they were reconstructed by a conventional 2D Filtered Back-Projection (FBP) algorithm in order to allow a comparison between 2D and 3D reconstructed images. A FBP algorithm was used in the following configurations

		Window	Cut-off
1	R	Rectangular	0.5
2	$H_{0.5}$	Hanning	0.5
3	$H_{0.33}$	Hanning	0.33
4	$H_{0.25}$	Hanning	0.25

- Condition 1 (R) allows the best resolution to be maintained in the images but with high noise particularly in the case of low counting statistics data.

- Condition 4 ( $H_{0.25}$ ) allows noise reduction, but compromising spatial resolution
- Conditions 2 ( $H_{0.5}$ ) and 3 ( $H_{0.33}$ ) represent intermediate solutions with respect to Conditions 1 and 4.

## 6. RESULTS

### 6.1 PHANTOM STUDIES

For all phantom studies, unless otherwise specified, results are reported for:

- the High counting Statistics (HS) studies

the Low counting Statistics (LS) studies

- PROMIS reconstruction in the three selected configurations (RR, HR, HH)

FORE reconstruction in the selected configurations (FR, FH)

#### 6.1.1 POINT SOURCES (PS)

The PS studies allowed the investigation of spatial resolution in scanner FOV. The PS data were analyzed in terms of Full Width Half Maximum (FWHM)

Tables 6.1 and 6.2 summarize FWHM for PROMIS and FORE, respectively. Better spatial resolution values are obtained in the case of FORE reconstruction.

	RR		HR		HH	
position	Rad	Tan	Rad	Tan	Rad	Tan
0,0	5.21	5.70	6.44	6.90	6.57	6.91
0,10	5.86	5.92	7.02	7.15	7.06	7.14
0,20	7.14	5.89	8.10	7.08	8.13	7.10

**Table 6.1** PS data reconstructed by PROMIS. FWHM values for radial and tangetial profiles

	FR		FH	
position	Rad	Tan	Rad	Tan
0,0	4.5	4.68	5.25	6.03
0,10	5.17	5.33	6.17	6.48
0,20	6.40	5.31	7.19	6.47

**Table 6.2** PS data reconstructed by FORE. FWHM values for radial and tangetial profiles

### 6.1.2 UNIFORM CYLINDRICAL PHANTOM (UCY)

The UCY phantom studies allowed the investigation of the behaviour of the reconstruction algorithms with respect to noise. The UCY phantom data were analyzed in terms of Coefficient of Variation (CV), which represents an index of image uniformity and thus of noise. The higher is the noise level in the reconstructed image, the higher the value of CV.

Graphs reported in Figure 6.1 and 6.2 show the value of mean value  $m$  and CV, respectively, as a function of the plane index, for the HS (left) and LS (right) study, reconstructed by PROMIS. The three reconstruction configurations (RR, HR, HH) yield similar results in terms of mean value  $m$ . After proper data normalization accounting for plane efficiency differences,  $m$  is constant over the axial FOV of the scanner. The increase of CV values at the most external planes is explained by the lower efficiency of the PET system at the axial edges of the FOV. CV is much higher, as expected, for the LS study than for the less noisy HS study. The different values of CV for the three reconstruction configurations reflect the different behaviour with respect to noise: high noise/high resolution for RR, balance between noise and resolution for HR, low noise/low resolution for HH.

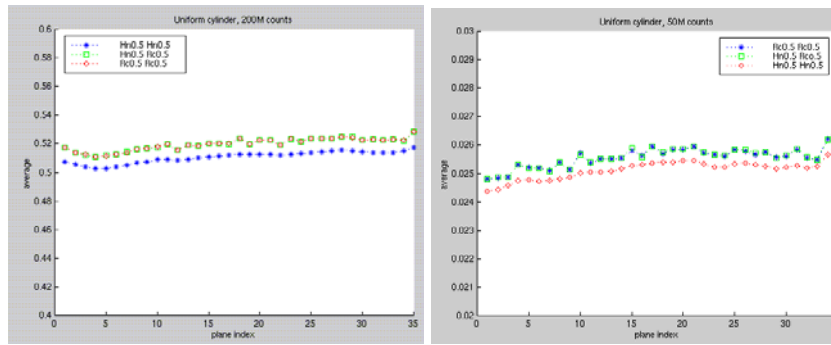


**Figure 6.1** UCY Phantom - PROMIS reconstruction: mean estimated activity  $m$  as a function of the plane number. HS study (left) and LS study (right)

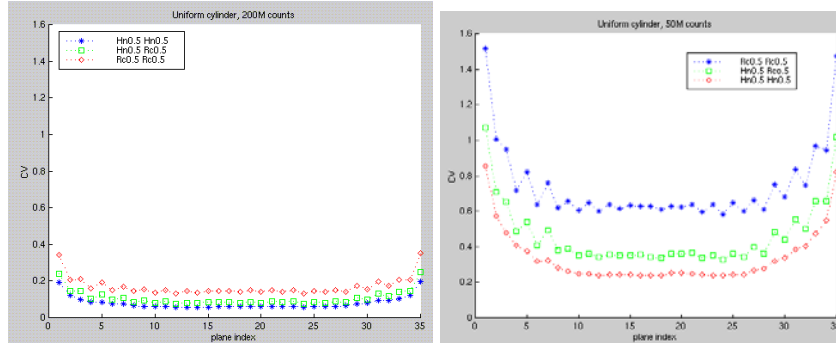


**Figure 6.2** UCY Phantom - PROMIS reconstruction: CV values as a function of the plane number. HS study (left) and LS study (right)

Table 6.3 summarizes the values of CV in a representative central plane (plane #10) for both HS and LS studies, reconstructed by PROMIS and FORE. The reconstruction algorithms with high resolution filters are penalized in terms of noise as demonstrated by the high CV values (e.g. PROMIS RR, FORE FR). A higher noise level is consistently found in FORE reconstructions.

	PROMIS			FORE	
	RR	HR	HH	FR	FH
HS	0.14	0.08	0.06	0.27	0.14
LS	0.61	0.34	0.24	1.16	0.58

**Table 6.3** UCY phantom: CV values in a representative plane (plane #10)

### 6.1.3 JASZCZAK PHANTOM

The JZA phantom allowed the investigation of the ability of the reconstruction algorithms to detect a cold lesion in a radioactive background. The different rod size in the six sectors of the JZA phantom allowed the study of the dependence of lesion detectability on the lesion size.

A representative image of the JZA phantom (slice#16) is shown in Figures 6.1 and 6.2 for the HS and LS studies reconstructed by PROMIS and FORE, respectively.

The smallest rod (size 4.5mm) is hard to recognize in all situations, due to spatial resolution and spill-over effects. A qualitative evaluation of the images prove that, although cold lesions are better defined in the high resolution images (e.g. PROMIS RR, FORE FR), noise is too high,

affecting lesion detectability. Very poor image quality was found for the LS images, reconstructed by FORE.

The JZA phantom was analyzed in terms of Contrast (C) as an index of lesion detectability.

Tables 6.4 and 6.5 summarize the values of C in a representative central plane (plane #16) for the HS and the LS study, respectively, for both PROMIS and FORE reconstruction algorithms.

For all reconstruction configurations, C decreases with the rod size. The sector with the smallest rods was not analyzed, as it was impossible to recognize the cold regions. C is consistently higher for both PROMIS and FORE with the high resolution filters (PROMIS RR and FORE FR). C values obtained by FORE are slightly better than with PROMIS.

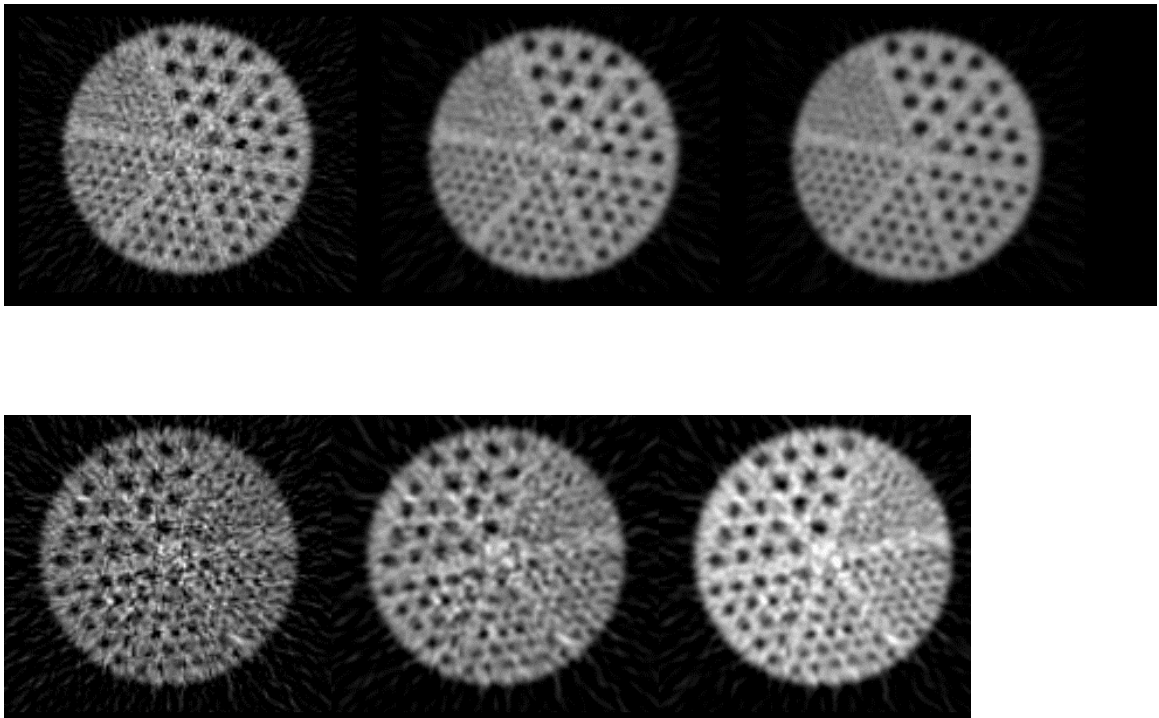


**Figure 6.3** *JZA phantom reconstructed by PROMIS (slice#16). HS study (top) and LS study (bottom). Reconstruction configurations: RR (left), HR (centre), HH (right)*

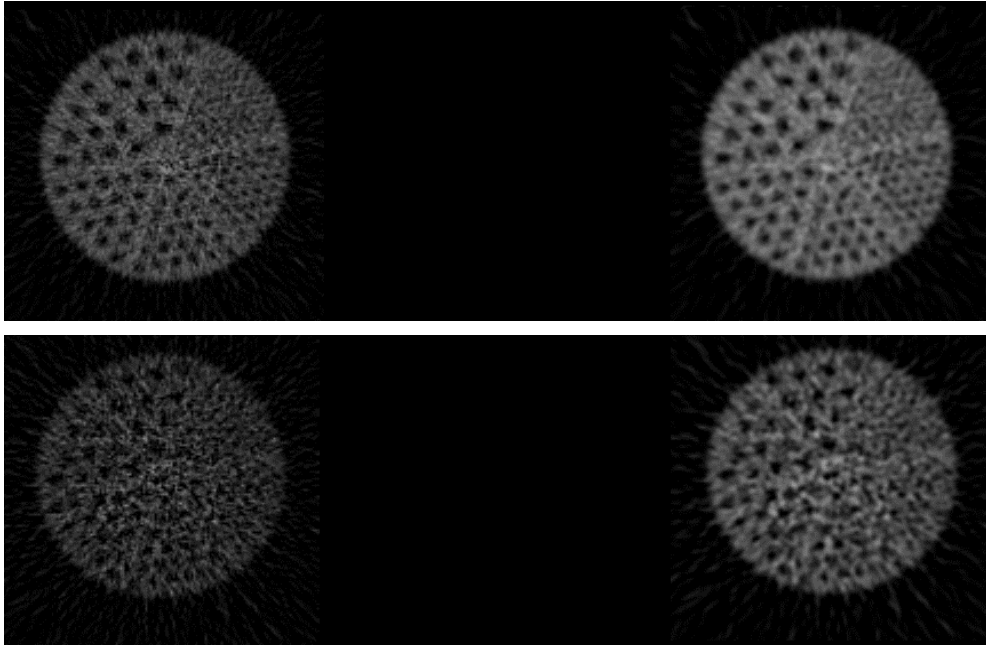


**Figure 6.4** *JZA phantom reconstructed by FORE. HS study (top) and LS study (bottom). Reconstruction configurations: FR (left), FH (right)*



	PROMIS			FORE	
Rods size (mm)	RR	HR	HH	FR	FH
12.7	0.81	0.75	0.75	0.83	0.76
11.1	0.78	0.70	0.69	0.83	0.76
9.5	0.74	0.64	0.64	0.77	0.68
7.9	0.69	0.55	0.55	0.70	0.59
6.4	0.59	0.45	0.44	0.68	0.53
4.5	-	-	-	-	-

**Table 6.4** JZA phantom, HS study (plane #16). C values for the six sectors

	PROMIS			FORE	
Rods size (mm)	RR	HR	HH	FR	FH
12.7	0.77	0.70	0.71	0.77	0.70
11.1	0.74	0.68	0.68	0.74	0.69
9.5	0.80	0.67	0.65	0.82	0.70
7.9	0.63	0.53	0.54	0.65	0.56
6.4	0.55	0.43	0.43	0.59	0.49
4.5	-	-	-	-	-

**Table 6.5** JZA phantom, LS study (plane #16). C values for the six sectors

#### 6.1.4 HOT SPHERE PHANTOM

The HS phantom studies allowed the investigation of the ability of the reconstruction algorithms to recognize a hot lesion in a radioactive background. The presence of spheres with different diameter at different radioactivity concentration ratio with respect to the background allowed a variety of situations to be covered.

A representative image of the HS phantom for the HS and LS studies is shown in Figures 6.7 and 6.8 for PROMIS and FORE reconstruction algorithms, respectively. As spheres in the phantom were not co-axial, not all spheres were visualized in a single slice. The cold small regions appearing in the right upper part of the images corresponds to plexiglass support for non

co-axial spheres. Although at a lower radioactivity concentration ratio (1.5), the larger spheres are better visualized, as less affected by resolution effects. In a qualitative evaluation, the LS study has very poor lesion detectability, in particular in FORE reconstruction.

The HS phantom was analyzed in terms of Radioactivity Concentration Ratio (RCR) between the radioactive spheres and the radioactive background.

Tables 6.6 and 6.7 summarize the values of RCR for HS and LS studies, respectively, for both PROMIS and FORE reconstructions. Estimated RCR decreases with sphere size. As an example, in PROMIS reconstructions (RR), in the larger spheres, RCR underestimation is on the order of  $\approx 5\%$ , in the two medium size spheres on the order of  $\approx 35\%$  and in the two smaller spheres on the order of  $\approx 55\%$ . FORE shows a similar behaviour. Some inconsistencies, particularly in the LS study, may be attributed to the high noise in the reconstructed images.

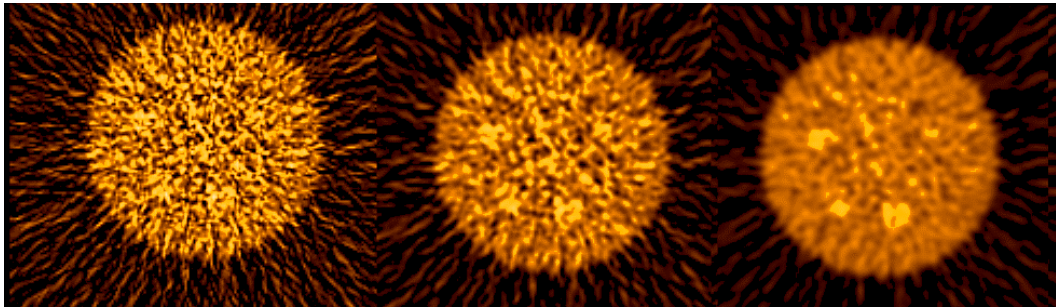
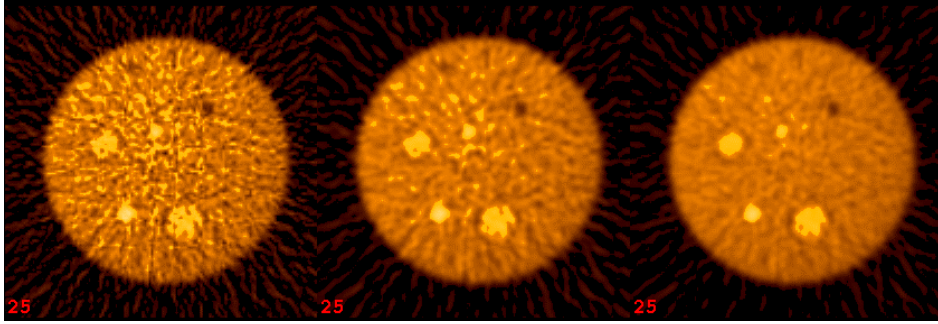


**Figure 6.7.** *HS phantom reconstructed by PROMIS. HS study (top) and LS study (bottom). Reconstruction configurations: RR (left), HR (centre), HH (right)*





**Figure 6.8.** *HS phantom reconstructed by FORE. LS study (top) and LS study (bottom).  
Reconstruction configurations: FR (left), FH (right)*

		PROMIS			FORE	
Sphere size (mm)	True ratio	RR	HR	HH	FR	FH
38.0	1.5	1.35	1.35	1.31	1.32	1.30
31.5	1.5	1.44	1.43	1.38	1.42	1.38
25.5	1.5	1.49	1.46	1.33	1.36	1.21
18.5.	2.8	1.64	1.59	1.53	1.75	1.70
16.0	2.8	1.94	1.88	1.70	1.71	1.69
13.0	3.6	1.66	1.61	1.46	1.54	1.47
9.5	3.6	1.43	1.41	1.31	1.20	1.23

**Table 6.6** *HS phantom, HS study. RCR values vs sphere size*

		PROMIS			FORE	
Sphere size (mm)	True ratio	RR	HR	HH	FR	FH
38.0	1.5	1.27	1.25	1.23	1.37	1.36
31.5	1.5	1.37	1.35	1.32	1.36	1.34
25.5	1.5	1.34	1.32	1.26	1.54	1.51
18.5.	2.8	1.77	1.69	1.63	1.89	1.82
16.0	2.8	2.03	1.91	1.77	1.84	1.75
13.0	3.6	1.77	1.66	1.48	1.90	1.77
9.5	3.6	1.58	1.48	1.38	1.44	1.40

**Table 6.7** *HS phantom, LS study. RCR values vs sphere size*

### 6.1.5 HOFFMAN BRAIN PHANTOM

The HB phantom allowed the investigation of the performance of the reconstruction algorithms in a situation similar to that of a cerebral PET study of glucose metabolism with  $^{18}\text{F}$ FDG or blood flow with  $\text{H}_2^{15}\text{O}$ , presenting with a complex radioactivity distribution in small anatomical structures.

A representative image of the HB phantom (slice#19) is shown in Figures 6.9 and 6.10 for the HS and LS studies reconstructed by PROMIS and FORE, respectively. A good definition of anatomical structures can be observed in all reconstructions. In particular, note how subcortical structures as well as cortical circonvolutions are well outlined in the HS study. FORE is less effective, particularly in the reconstruction of the LS study.

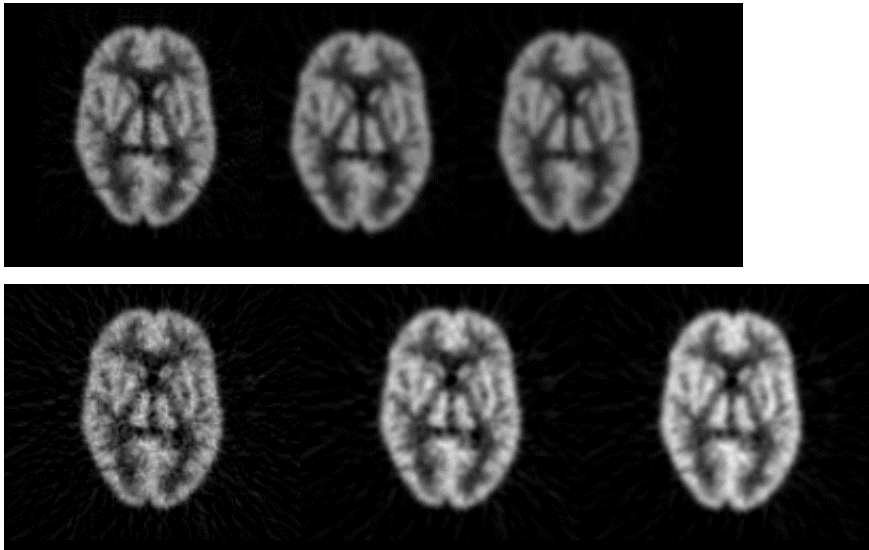


**Figure 6.9** *HB phantom reconstructed by PROMIS. HS study (top) and LS study (bottom). Reconstruction configurations: RR (left), HR (centre), HH (right)*

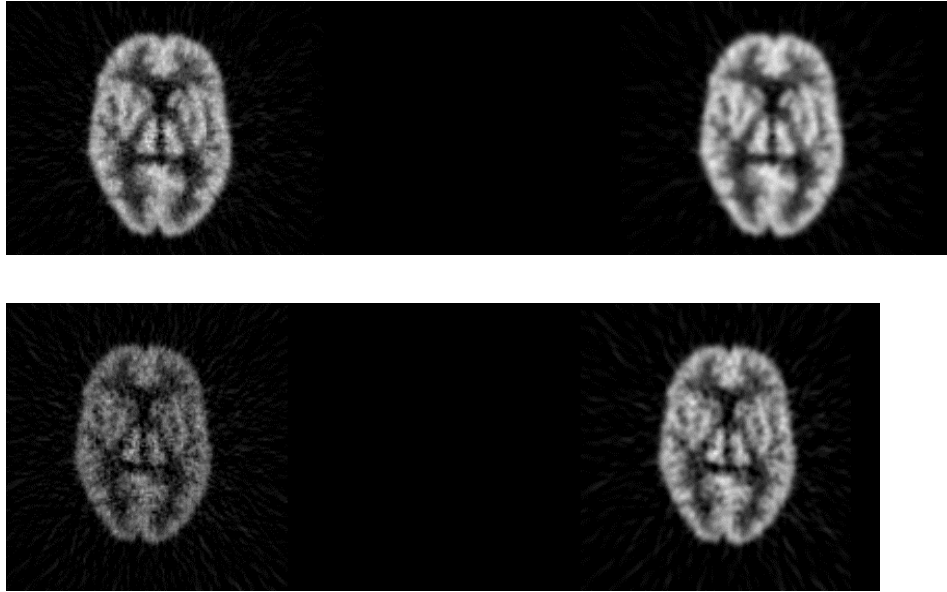


**Figure 6.10** *HB phantom reconstructed by FORE. HS study (top) and LS study (bottom). Reconstruction configurations: FR (left), FH (right)*

The HB phantom was analyzed in terms of Radioactivity Concentration Ratio (RCR) between Gray Matter (GM) and White Matter (WM) and in terms of Contrast (C) in the Cerebrospinal Fluid with respect to Gray Matter. Tables 6.8 and 6.9 summarize the values of RCR and C in two representative central planes (plane #19 and 24) for HS and LS studies, respectively, for both PROMIS and FORE reconstructions. The theoretical value for GM : WM RCR is 4. The theoretical value for C is 1. For both RCR and C, comparable results are obtained in the HS and LS studies. Similar values of GM:WM RCR are obtained in the two selected slices. Better results are obtained in images reconstructed by PROMIS and FORE with high resolution filters (e.g. PROMIS RR, FORE FR), less affected by partial volume and spill-over effects. RCR values obtained by FORE are slightly better than with PROMIS.

Slice	RCR	PROMIS			FORE	
		RR	HR	HH	FR	FH
#19	GM : WM	3.11	2.99	2.72	3.30	3.15
#24	GM : WM	3.27	3.11	2.98	3.22	3.18
#24	C	0.87	0.856	0.84	0.89	0.87

**Table 6.8** *HB Phantom, HS study: RCR and C values calculated in GM, WM and CSF*

		PROMIS			FORE	
Slice	RCR	RR	HR	HH	FR	FH
#19	GM : WM	3.2285	3.0468	2.8207	3.4129	3.2870
#24	GM : WM	3.3869	3.0872	2.9598	3.8100	3.3729
#24	C <sub>CSF</sub>	0.875	0.848	0.832	0.869	0.849

**Table 6.9** *HB Phantom, LS study: RCR  $C_{CSF}$  values calculated in GM, WM and CSF*

### 6.1.6 STRIATA PHANTOM

The ST phantom allowed the investigation of the performance of the reconstruction algorithms in a situation similar to that of a cerebral PET study of neurotransmission system (e.g.  $^{18}\text{F}$ ESF) presenting with high uptake of the radiotracer in the basal ganglia (putamen and caudate) and low uptake in the surrounding anatomical structures (background). Results are reported for the single study available for this phantom ( $\approx 33$  Mcounts).

A representative image of the ST phantom (slice#17) is shown in Figures 6.11 and 6.12 reconstructed by PROMIS and FORE, respectively. Although with good anatomical definition, the FORE images appear more noisy than PROMIS.

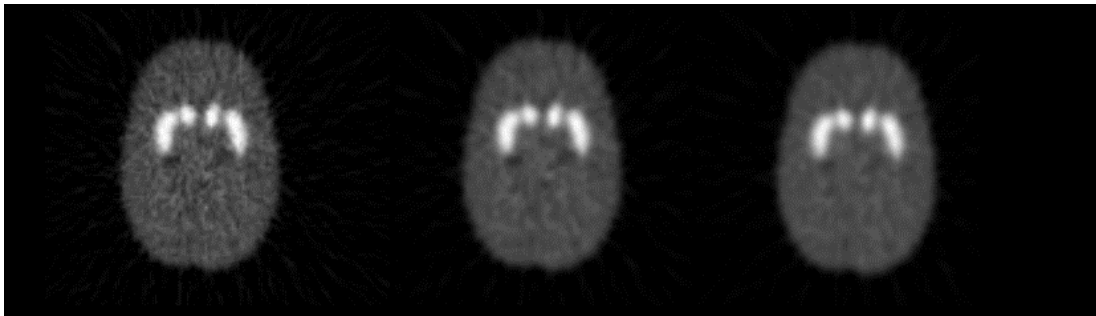


**Figure 6.11** *ST phantom reconstructed by PROMIS. Reconstruction configurations: RR (left), HR (centre), HH (right)*

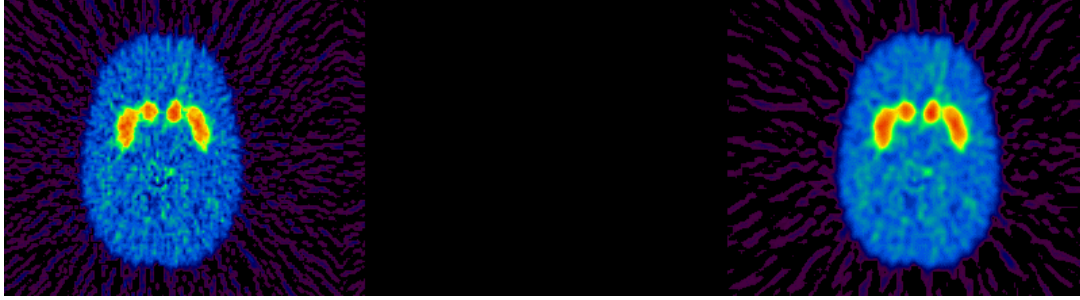


**Figure 6.12** *ST phantom reconstructed by FORE. Reconstruction configurations: FR (left), FH (right)*

The ST phantom was analyzed in terms of Radioactivity Concentration Ratio (RCR) in the putamen and caudate compartments with respect to the surrounding background (bkg). Table 6.10 summarizes the values of RCR in the representative central plane (plane #17), for PROMIS and FORE reconstructions in all configurations considered. The true value of RCR is 3.84. Putamen:bkg ratio is consistently higher than caudate:bkg ratio as a result of partial volume effect, more affecting the caudate compartment with a smaller size than the putamen. Both Putamen:bkg and caudate:bkg RCR values are consistently higher, for both PROMIS and FORE, in the case of the high resolution filters (PROMIS RR and FORE FR). RCR values obtained by FORE are slightly better than with PROMIS.

Slice	RCR	PROMIS			FORE	
		RR	HR	HH	FR	FH
#17	Putamen : bkg	3.46	3.01	2.88	3.55	3.38
#17	Caudate : bkg	3.10	2.50	2.42	3.48	3.26

**Table 6.10** *ST Phantom. RCR values calculated in the caudate and putamen with respect to background*

### 6.1.7 HEART PHANTOM

The H phantom studies allowed the investigation of the performance of the reconstruction algorithms in a situation similar to that of a heart PET study (e.g. with  $^{18}\text{F}$ FDG).



A representative image of the H phantom (slice#20) is shown in Figures 6.13 and 6.14 for the HS and LS studies reconstructed by PROMIS and FORE, respectively. In the HS study, high quality images can be observed for all reconstruction configurations: the phantom compartments can be clearly identified, including the thin plexiglass thickness separating the compartments. The high level of noise in the LS study, heavily affecting image quality, is explained by the very low counting statistics (5 Mcounts). A qualitative comparison between PROMIS and FORE shows the higher noise present in the FORE images.

The H phantom was analyzed in terms of Radioactivity Concentration Ratio (RCR) between Left Ventricle (LV) wall and cavity and in terms of Contrast (C) in the cold lesion with respect to LV wall.

Table 6.11 summarizes the values of RCR and C in the representative central plane (plane #20) for HS and LS studies, for all PROMIS and FORE reconstructions. RCR and C are consistently higher for both PROMIS and FORE with the high resolution filters (PROMIS RR and FORE FR). RCR and C values obtained by FORE are slightly better than with PROMIS.

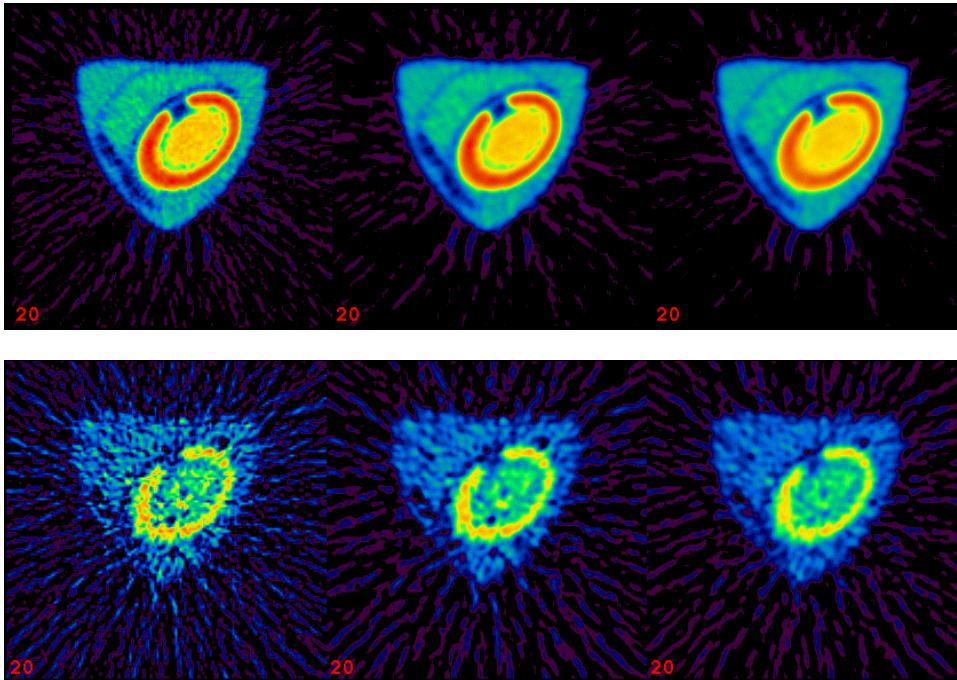


**Figure 6.13** Heart phantom reconstructed by PROMIS. HS study (top) and LS study (bottom). Reconstruction configurations: RR (left), HR (centre), HH (right)

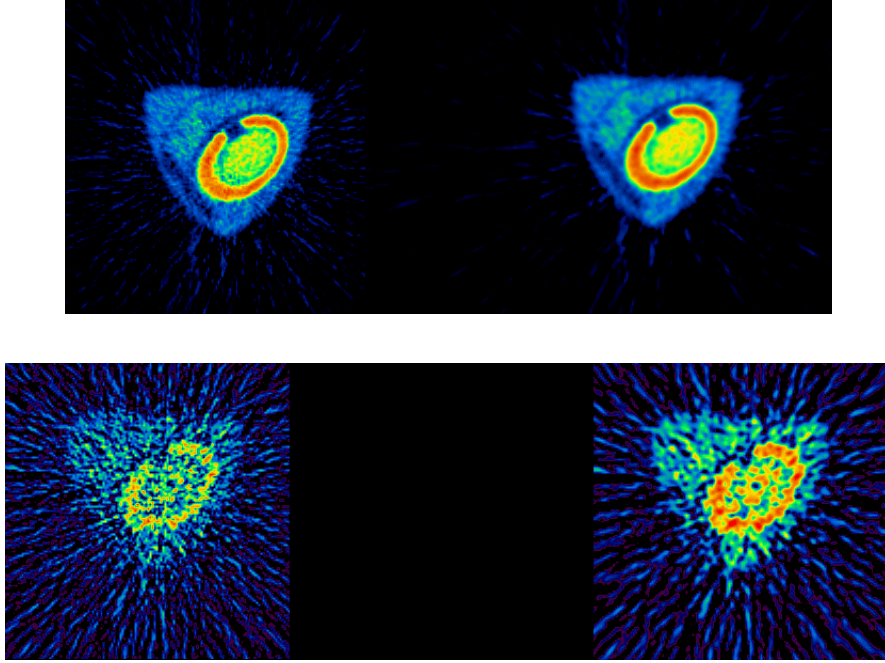


**Figure 6.14** Heart phantom reconstructed by FORE. HS study (top) and LS study (bottom). Reconstruction configurations: FR (left), FH (right)

Slice#20		True RCR	PROMIS			FORE	
			HH	HR	RR	FH	FR
HS	LV W:Ca	1.74	1.56	1.62	1.67	1.66	1.70
HS	C	3.64	0.92	0.91	0.88	0.93	0.91
LS	LV W:Ca	1.74	1.51	1.52	1.52	1.63	1.67
LS	C	3.64	0.82	0.81	0.80	0.90	0.89

**Table 6.11** Heart phantom. RCR values calculated in the LV wall with respect to LV cavity (LV W:Ca)

### 6.1.8 WHOLE BODY PHANTOM

The Whole Body phantom studies allowed the investigation of the performance of the reconstruction algorithms in a situation similar to that of a  $^{18}\text{F}$ FDG Whole Body PET study.

Four representative images of the Whole Body phantom study (slices#9, 13, 20 and 26) are shown in Figures 6.15 and 6.16, reconstructed by PROMIS and FORE, respectively. Images in this study are characterized by a low distributed background radioactivity and by small regions with high radioactivity concentration ratio with respect to background (7.5 in this experiment). This situation results in a high noise component in the background, while lesion detectability is strongly dependent on lesion size. A qualitative evaluation of PROMIS and FORE image quality is in favour of PROMIS: in particular the three smaller regions, visualized in the PROMIS reconstructed images, are hardly recognized by FORE.

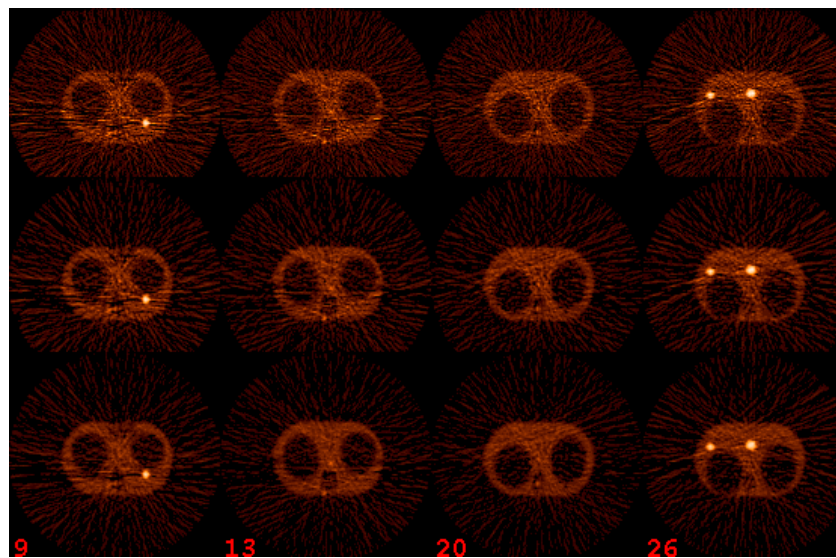


**Figure 6.15** *Whole Body phantom reconstructed by PROMIS. Reconstruction configurations: RR (top row), HR (central row), HH (bottom row)*

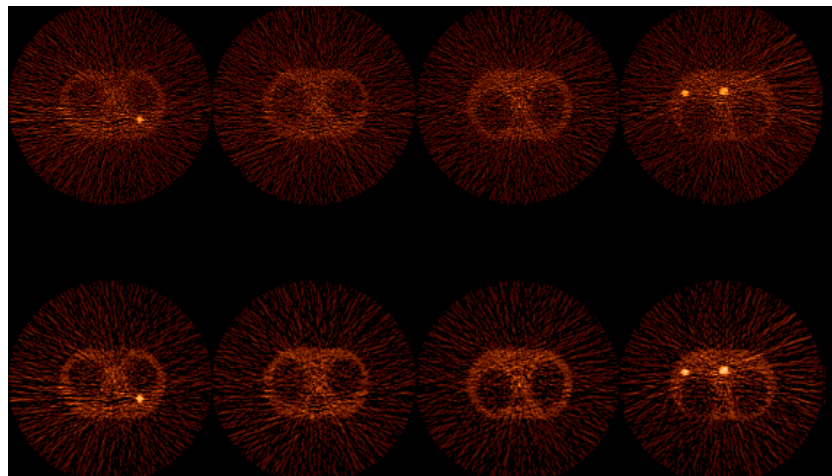


**Figure 6.16** *Whole Body phantom reconstructed by FORE. Reconstruction configurations: FR (top row), HH (bottom row)*

Table 6.12 summarizes values of RCR calculated for the six spheres on PROMIS and FORE images. The true value of RCR was 7.5. Measured RCR values underestimate true RCR value as a result of resolution effects. PROMIS and FORE behave similarly. In particular, although by visual inspection the radioactive spheres are better visualized in PROMIS images, RCR values are comparable.

	PROMIS			FORE	
Sphere size (mm)	RR	HR	HH	FR	FH
38.0	6.41	6.00	5.46	6.15	5.87
31.5	5.74	5.69	5.18	5.91	5.92
25.5	4.73	4.58	4.32	4.60	4.50
16.0	2.06	2.00	1.74	2.17	2.13
13.0	1.94	1.91	1.91	2.19	2.12
9.5	1.80	1.71	1.54	1.83	1.76

**Table 6.12** *Whole Body phantom. RCR values calculated for the six spheres in the phantom*

## 6.2 CLINICAL DATA

### 6.2.1 BRAIN STUDIES OF GLUCOSE METABOLISM ( $^{18}\text{F}$ FDG)

The patient in this study was affected by brain tumor and had been previously treated by radiotherapy. The  $^{18}\text{F}$ FDG PET study was performed to allow the differentiation between tumor recurrence and radionecrosis. Figure 6.17 shows two representative slices (slices #18 and 19) of the 2D PET  $^{18}\text{F}$ FDG study, reconstructed by 2D FBP reconstruction algorithm. Figure 6.18 and 6.19 show the correspondent 3D PET images (same representative slices), reconstructed by PROMIS and FORE, respectively. A reduced metabolic activity is evident in all images in the right temporo-parietal region, in correspondence to necrotic tissue resulting from the radiotherapeutic treatment. Within this area, a region of high metabolic activity is recognized, relative to tumor recurrence. As a result of the high counting

statistics of the 3D with respect to the 2D PET study (200 Mcounts vs 40 Mcounts), 3D image quality is much superior, particularly in terms of statistical noise. In the comparison between PROMIS and FORE images, the general trend of more noisy FORE images is confirmed.

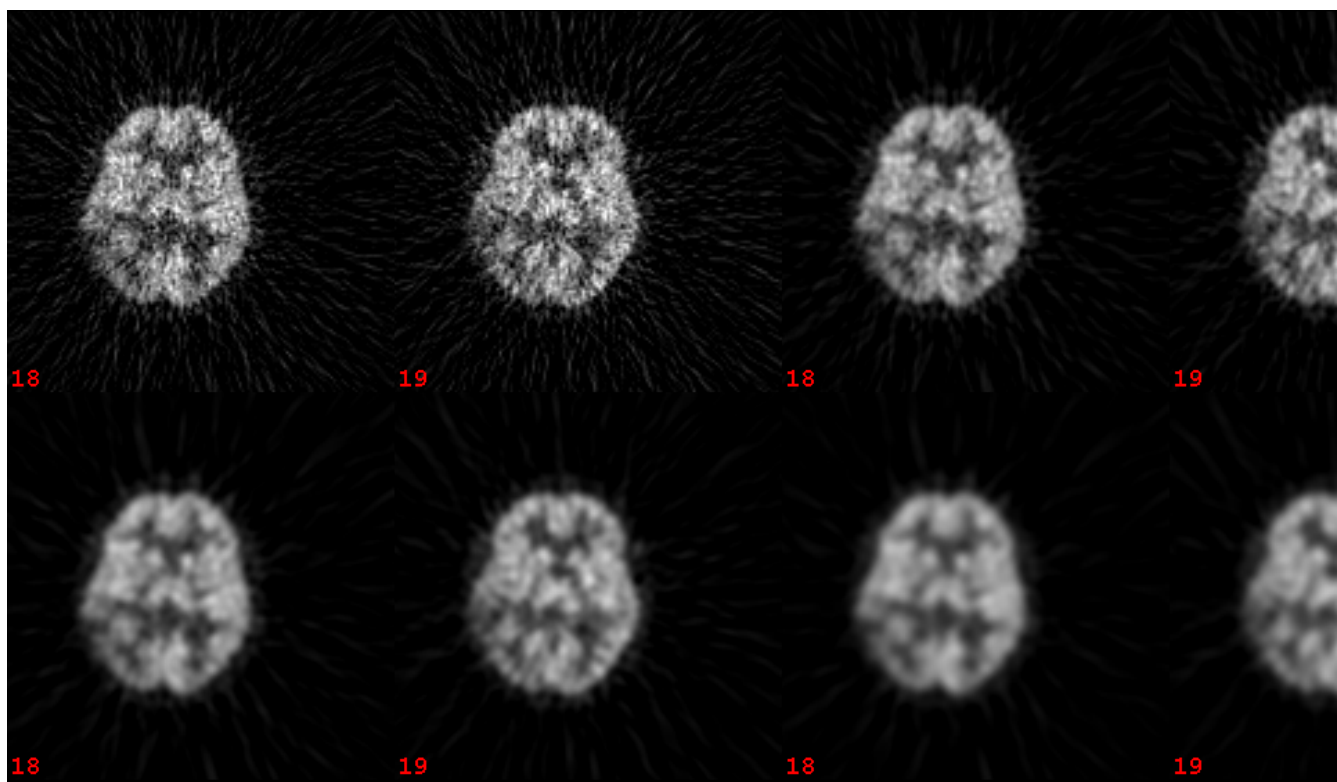


**Figure 6.17** 2D  $^{18}\text{F}$ FDG brain PET study of glucose metabolism - Two representative slices (slices#18 and 19). 2D FBP reconstruction: R (top left),  $H_{0.5}$  (top, right),  $H_{0.33}$  (bottom left),  $H_{0.25}$  (bottom right)

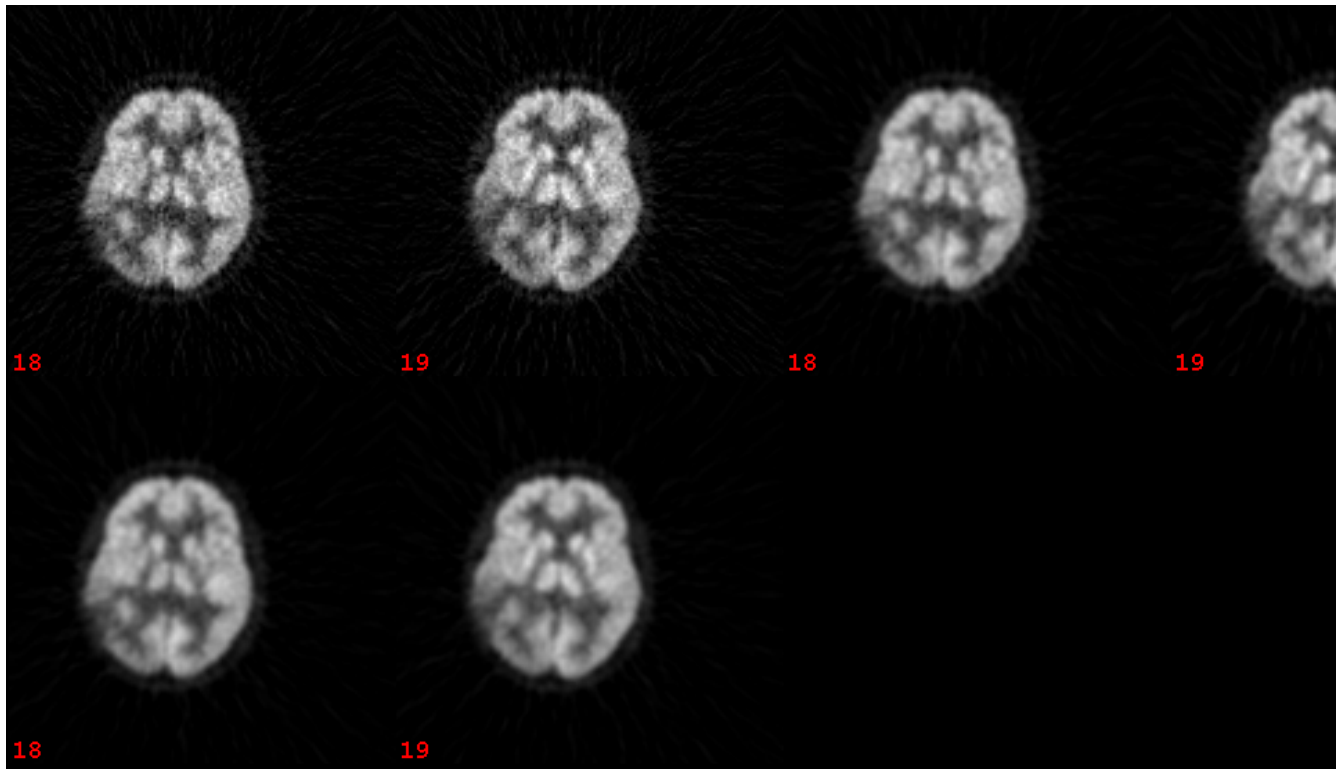


**Figure 6.18** 3D  $^{18}\text{F}$ FDG brain PET study of glucose metabolism - Two representative slices (slices#18 and 19). PROMIS reconstruction: RR (top, left), HR (top, right), HH (bottom, left).

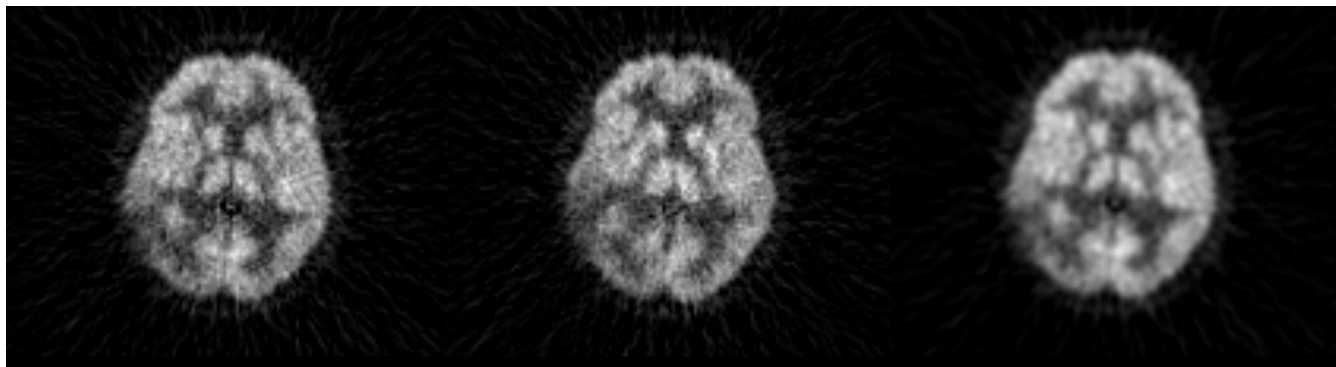


**Figure 6.19** 3D  $^{18}\text{F}$ FDG brain PET study of glucose metabolism - Two representative slices (slices#18 and 19). FORE reconstruction: FR (first 2 images-left), FH (last 2 images-right)



This brain study of glucose metabolism with  $^{18}\text{F}$ FDG was analyzed in terms of Radioactivity Concentration Ratio (RCR) in the Gray Matter with respect to White Matter and with respect to the pathological lesion. Results are presented for a) the 3D study reconstructed by PROMIS (RR, HR, HH), b) the 3D study reconstructed by FORE (FR, FH), c) the 2D study reconstructed by 2D FBP (R,  $H_{0.5}$ ,  $H_{0.33}$ ,  $H_{0.25}$ )

Table 6.13 summarizes the values of RCR in a representative plane (plane #18) for the 2D and 3D studies. RCR and C values are in agreement with the results found in the HB phantom study (reproducing the situation of a  $^{18}\text{F}$ FDG brain study). In particular, an underestimation of RCR with respect to the expected value of 4 is observed, due to partial volume and spill-over effects. RCR and C values are not as affected by the choice of filter as in the case of the HB phantom. This may be due to the fact that in clinical studies, the radioactivity is not distributed as precisely as in phantom studies: this implies that tissue heterogeneity effect within the defined ROIs can dominate over resolution effect and thus filter dependence.

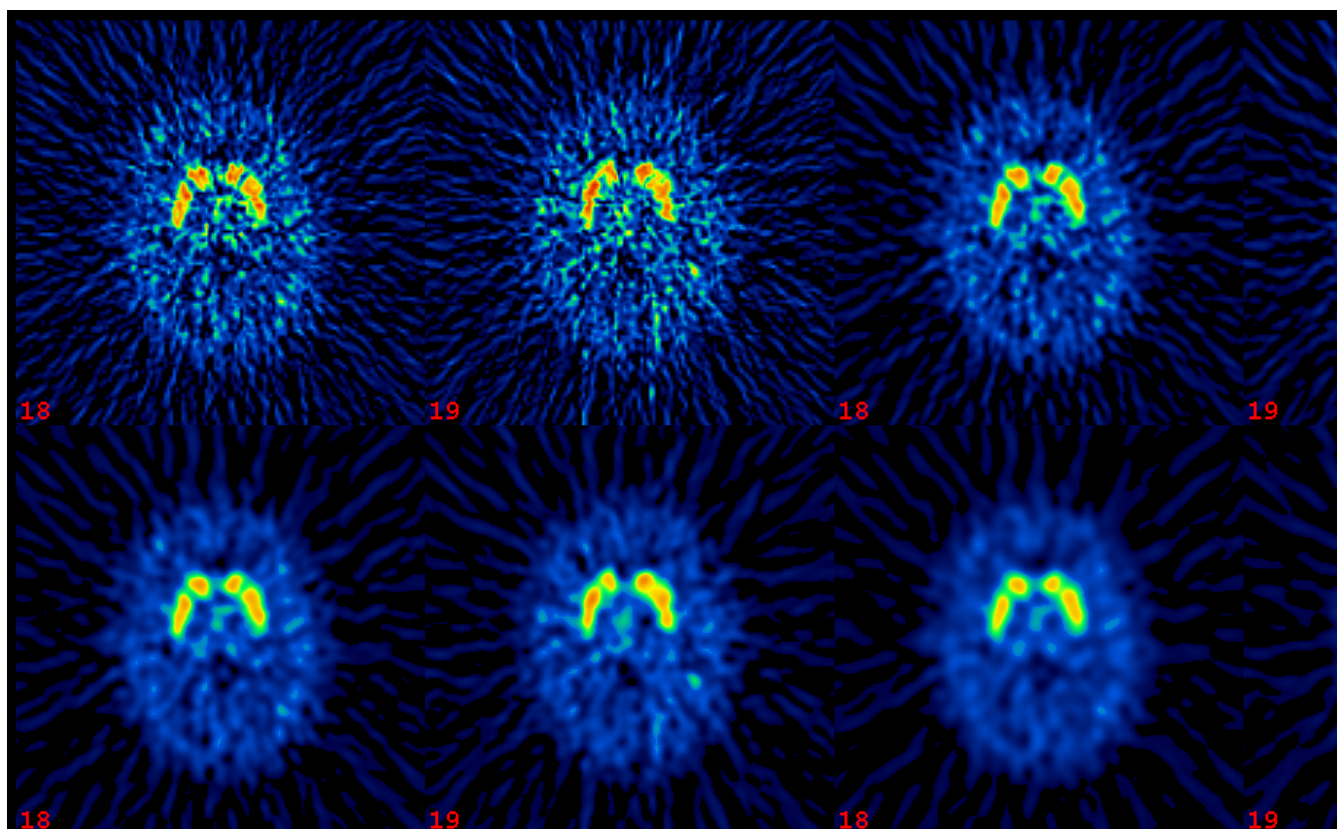
		3D					2D			
		PROMIS			FORE		FBP			
Slice#18		RR	HR	HH	FR	FH	R	$H_{0.5}$	$H_{0.33}$	$H_{0.25}$
2D	C						0.55	0.54	0.53	0.51
2D	GM:WM						2.53	2.48	2.40	2.29
3D	C	0.56	0.55	0.56	2.37	2.31				
3D	GM:WM	2.50	2.44	2.36	2.49	2.43				

Table 6.13  $^{18}\text{F}$ FDG brain PET study of glucose metabolism - RCR values

## 6.2.2 BRAIN STUDIES OF NEUROTRANSMISSION SYSTEMS ( $^{18}\text{F}$ FESP)

$^{18}\text{F}$ FESP is a tracer of the  $\text{D}_2$  dopaminergic receptors, principally localized in the basal ganglia, and of the  $5\text{HT}_2$  serotonergic receptors, prevalent in the cortical structures. Figure 6.20 reports a 2D PET  $^{18}\text{F}$ FESP study in a normal subject. Two representative slices are shown (slices#18 and 19), reconstructed by the 2D FBP algorithms. Figure 6.21 and 6.22 report the correspondent 3D PET study (same representative slices), reconstructed by PROMIS and FORE, respectively.

Note the improved signal/noise ratio in 3D images, the improved spatial resolution, allowing better differentiation of anatomical structures within the brain striata (putamen and caudate), and the visualization of the cortex, possible only in 3D images.



**Figure 6.20** 2D  $^{18}\text{FESP}$  brainPET study of neurotransmission. Two representative slices (slices#18 and 19). 2D FBP reconstruction:  $R_{0.5}$  (top left),  $H_{0.5}$  (top, right),  $H_{0.76}$  (bottom left),  $H_1$  (bottom right)



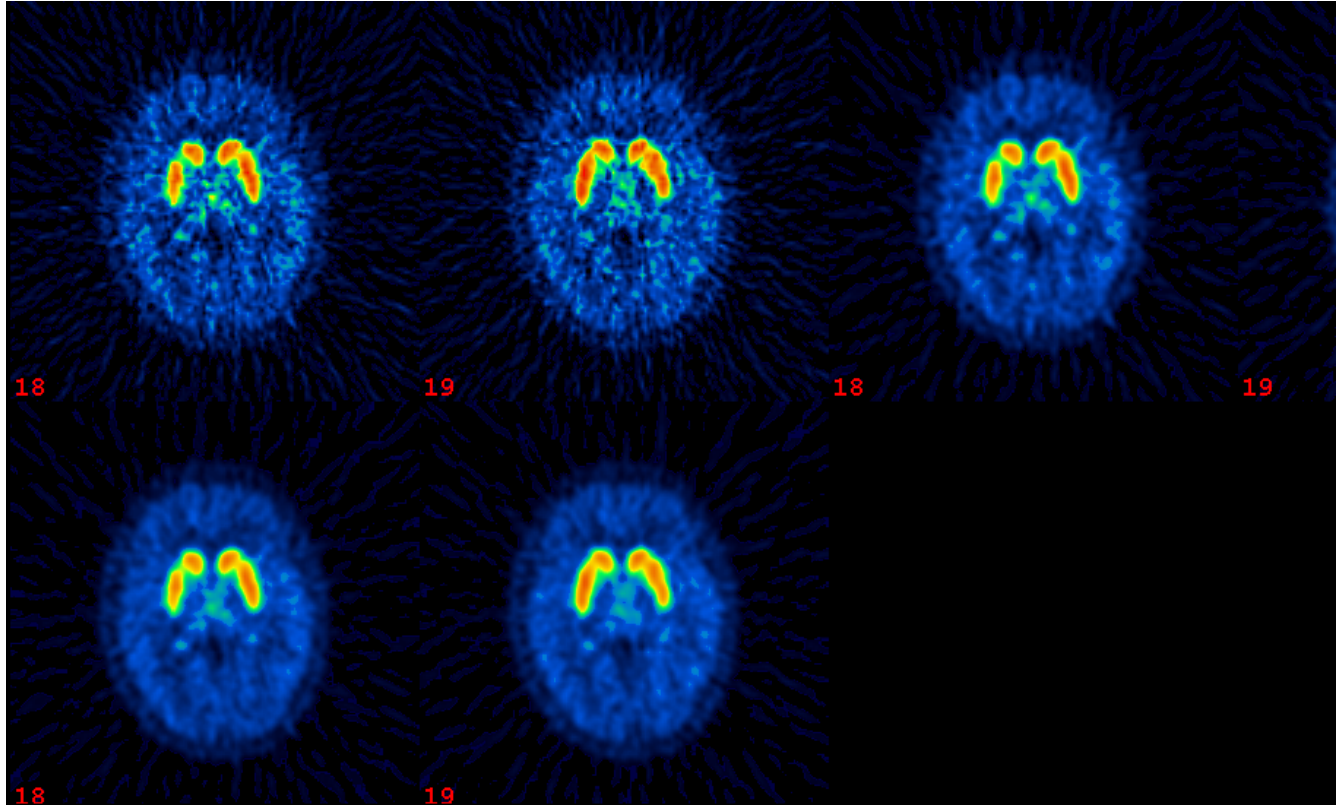


**Figure 6.21** 3D  $^{18}\text{F}$ ESP brain PET study of neurotransmission. Two representative slices (slices#18 and 19). PROMIS reconstruction: RR (top, left), HR (top, right), HH (bottom, left)

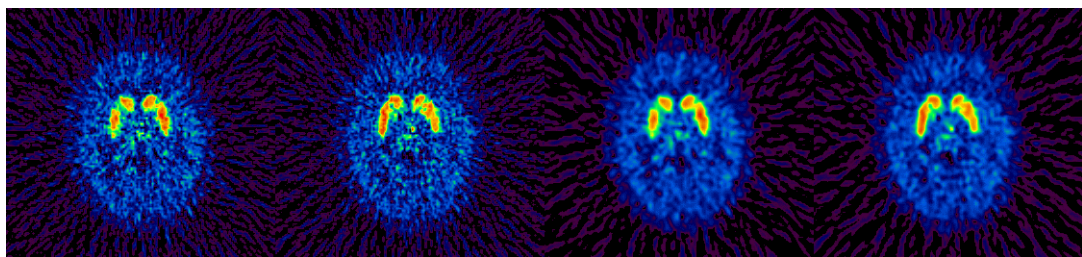


**Figure 6.22**  $^{18}\text{F}$ ESP brain 3D PET study of neurotransmission. Two representative slices (slices#18 and 19). FORE reconstruction: FR (left), FH (right)

This brain study of neurotransmission with  $^{18}\text{F}$ FESP was analyzed in terms of RCR in the basal ganglia with respect to cerebellum (Binding Index, BI). Results are presented for the 3D study reconstructed by (RR, HR, HH) and FORE (FR, FH), for the 2D study reconstructed by 2D FBP (R,  $H_{0.5}$ ,  $H_{0.33}$ ,  $H_{0.25}$ )

Table 6.14 summarizes the values of BI in a representative plane (plane #18) for the 2D and 3D studies, for all reconstruction configurations considered. Average value for BI in normal subjects is on the order of 6. Values of the BI in 3D data are higher than in 2D. This can be explained by the different time at which the 2D and 3D studies have been performed. In fact, the radiotracer distribution changes with time and the uptake of  $^{18}\text{F}$ FESP in the basal ganglia increases while radioactivity in the background decreases. The 2D study was performed first and thus measuring a lower BI than the following 3D study. PROMIS and FORE values are comparable.

	3D					2D			
	PROMIS			FORE		FBP			
Slice#18	RR	HR	HH	FR	FH	R	$H_{0.5}$	$H_{0.33}$	$H_{0.25}$
2D						7.03	5.78	6.22	6.63
3D	7.65	7.25	6.88	7.66	7.32				

**Table 6.14**  $^{18}\text{F}$ FESP brain 3D PET study of neurotransmission - BI values

### 6.2.3 HEART STUDIES OF GLUCOSE METABOLISM ( $^{18}\text{F}$ FDG)

The patient in this study was affected by anterior myocardial infarction. The  $^{18}\text{F}$ FDG PET study was performed to allow the assessment of myocardial viability. Figure 6.23 and 6.24 show two representative images of the 3D PET study, reconstructed by PROMIS and FORE, respectively. The myocardial anatomy is clearly outlined (left and right ventricle walls, septum, papillary muscles), the uptake of the radiotracer proving viability of the myocardial tissue. An ischemic lesion can be seen in the antero-septal wall. A ventricle dilation is also evident, as a result of the coronaric disease. The general trend of noisy FORE images is confirmed.

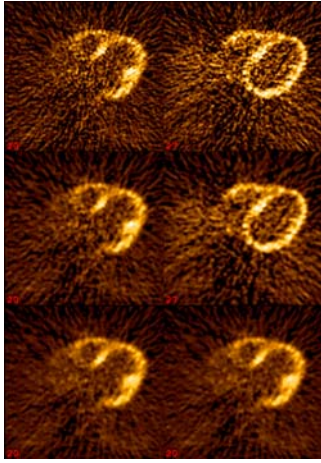


**Figure 6.23** 3D  $^{18}\text{F}$  FDG heart PET study of glucose metabolism. Two representative slices (slices#20 and 27). PROMIS reconstruction: RR (top), HR (centre), HH (bottom).

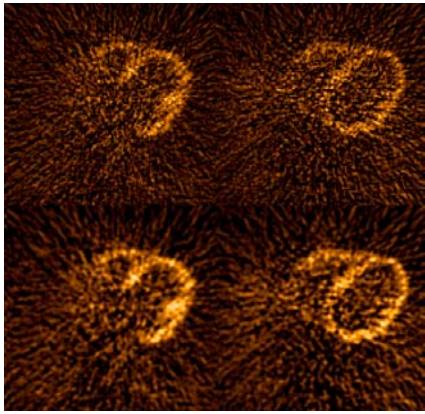


**Figure 6.24** 3D  $^{18}\text{F}$  FDG heart PET study of glucose metabolism. Two representative slices (slices#20 and 27). PROMIS reconstruction: RR (top), HR (centre), HH (bottom).

Table 6.15 summarizes the values of RCR and C in a representative plane for PROMIS and FORE reconstruction. Comparable results are obtained for PROMIS and FORE.

	PROMIS			FORE	
	RR	HR	HH	FR	FH

C	0.20	0.21	0.23	0.18	0.18
LV W:Ca	4.73	4.39	4.45	4.94	4.65

**Table 6.15** 3D  $^{18}\text{F}$ FDG heart PET study of glucose metabolism - RCR and C values

#### 6.2.4 WHOLE BODY STUDIES OF GLUCOSE METABOLISM ( $^{18}\text{F}$ FDG)

A PET  $^{18}\text{F}$ FDG whole-body study allows the assessment of glucose metabolism in the human body for the detection of primary tumours as well as of metastatic lesions. Figure 6.25 shows four representative slices from a PET  $^{18}\text{F}$ FDG whole-body study acquired in the 2D mode. Figure 6.26 and 6.27 report the correspondent 3D PET study (same representative slices), reconstructed by PROMIS and FORE, respectively. In this case, the PET whole body study allowed the detection of a solitary pulmonary nodule in the right upper lobe. The high metabolic activity in the pathological lesion is related to the malignancy of the nodule. Counting statistics in these studies is very poor (7 Mcounts and 30 Mcounts in 2D and 3D, respectively) and radioactivity is localized in the small pathological lesion, surrounded by a low activity distributed background. The resulting images, independently on the acquisition modality (2D, 3D) and on the reconstruction method used (PROMIS, FORE) are of very poor quality, very affected by noise. Iterative methods are expected to improve image quality particularly in  $^{18}\text{F}$ FDG whole-body study.

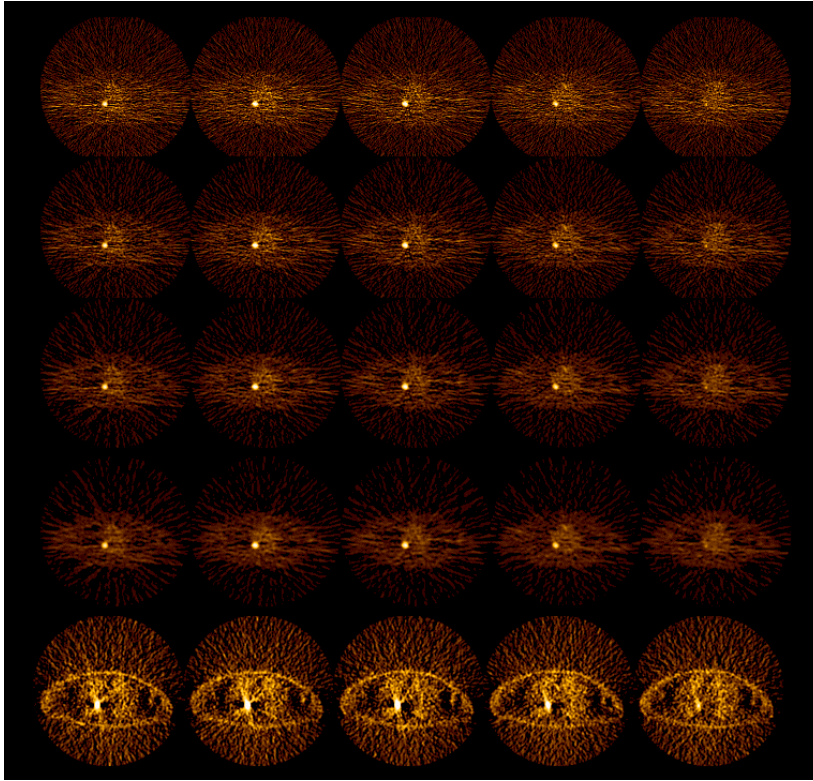


**Figure 6.25** 2D  $^{18}\text{F}$ FDG Whole Body PET study of glucose metabolism. Five representative slices (slices#). 2D FBP reconstruction:  $R_{0.5}$  (1st row),  $H_{0.5}$  (2nd row),  $H_{0.33}$  (3rd row),  $H_{0.25}$  (4rd row),  $H_{0.25}$  with attenuation correction (5th row)

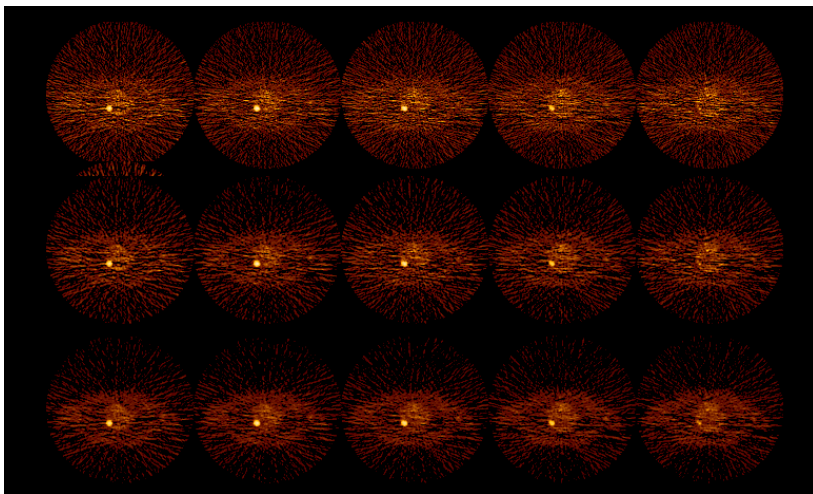


**Figure 6.26** 3D  $^{18}\text{F}$ FDG Whole Body PET study of glucose metabolism. Five representative slices (slices#). PROMIS reconstruction: RR (1st row), HR (2nd row), HH (3rd row)

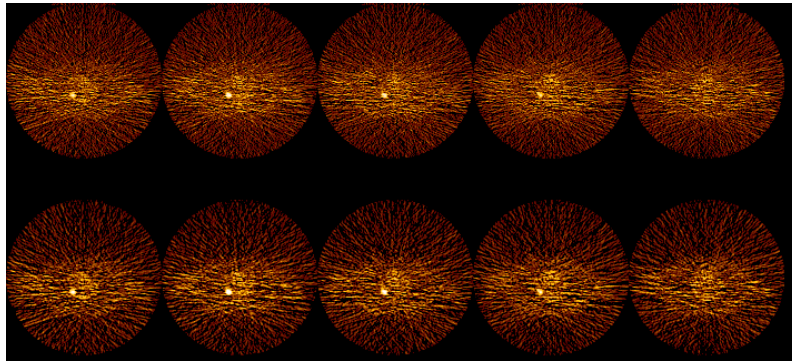


**Figure 6.27** 3D  $^{18}\text{F}$ FDG Whole Body PET study of glucose metabolism. Five representative slices (slices#). FORE reconstruction: FR (1st row), FH (2nd row)

Table 6.16 summarizes the results in terms of RCR in the pathological lesions with respect to background, demonstrating the high contrast characterizing these images. PROMIS and FORE behave similarly.

	3D					2D			
	PROMIS			FORE		FBP			
	RR	HR	HH	FR	FH	R	H <sub>0.5</sub>	H <sub>0.33</sub>	FH
2D L1						10.65	10.31	9.91	9.34
2D L2						19.87	19.46	18.90	18.05
3D L1	9.53	9.76	10.29	9.92	9.35				
3D L2	25.52	25.53	26.22	25.40	25.77				

**Table 6.16** 3D  $^{18}\text{F}$ FDG heart PET study of glucose metabolism - RCR and C values



## 7 CONCLUSIONS

The two analytic algorithms PROMIS and FORE were evaluated. For both algorithms different combinations of reconstruction parameters were considered (reconstruction filter, frequency cut-off). Evaluation was performed qualitatively by visual inspection of image quality and quantitatively by estimation of FOMs, specific for each evaluation study. In particular Coefficient of Variation (CV) was measured as an index of image uniformity (noise content), Contrast and Radioactivity Concentration Ratios (RCR) were estimated to assess lesion detectability.

The results of the comparison between PROMIS and FORE can be summarized as follows:

- PROMIS performs better than FORE in terms of noise (lower CV values in regions of constant activity, e.g. uniform cylindrical phantom)
- FORE shows a slightly better values of contrast and RCR in all phantom and clinical studies considered for evaluation (e.g. Jaszczak phantom, Hoffman brain phantom,  $^{18}\text{F}$ FDG brain studies,  $^{18}\text{F}$ FDG Whole Body studies)
- Although contrast is slightly lower, image quality is generally better for PROMIS reconstructed images, as a result of the lower noise
- The better PROMIS image quality is particularly evident in low counting statistics studies, characterized by high noise content.

In terms of computing time, FORE is approximately 3 times faster than PROMIS. This represents a crucial factor in the choice of FORE as 3D reconstruction algorithm in a clinical environment.

The improvement of image quality in 3D PET studies was confirmed with respect to 2D, particularly in brain-like sources. The quality of whole body studies reconstructed by analytic algorithms was very poor both in 2D and 3D modality.

This finding of poor performance of the analytic algorithm in case of noisy data (e.g. whole body studies) confirms the need for implementing fast 3D iterative algorithms, according to the aims of the PARAPET project.



## 8. REFERENCES

- [Def97] Defrise M, Kinahan P E, Townsend D W, Michel C, Sibomana M and Newport D F **(1997)** Exact and approximate rebinning algorithms for 3-D PET data. *IEEE Trans. Med. Imaging*, MI-16: 145-158.
- [Kin89] Kinahan P E and Rogers J G **(1989)** Analytic 3D image reconstruction using all detected events. *IEEE Trans. Nucl. Sci.*, 36: 964-968.
- [PAR1.2] Thielemans K **(1998)** Specification of Simulated, Phantom and Clinical Data. Test Sets for the PARAPET project. *PARAPET documentation for D1.2, Hammersmith Hospital*.
- [PAR3.2] Belluzzo D, Bettinardi V and Gilardi M C **(1997)** Library of Experimental Phantom and Clinical Data (User Guide). *PARAPET documentation for D3.1, Hospital San Raffaele*.
- [PAR4.2] Labbe C, Zaidi H and Morel C **(1998)** Specification of PROMIS Building Blocks. *PARAPET documentation for D4.2b, Geneva University Hospital*.
- [PAR4.3] Labbe C, Zaidi H and Morel C **(2000)** Specification of FORE Building Blocks. *PARAPET documentation for D4.3, Geneva University Hospital*.